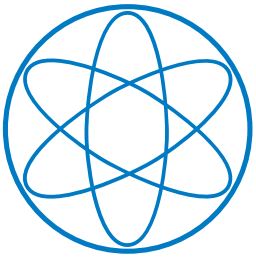

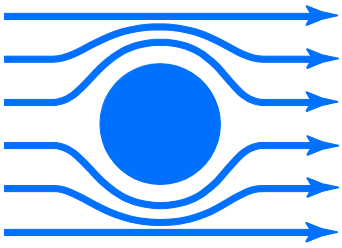

Physik-Department
Lehrstuhl E23

Walther-Meissner-Institut
für Tieftemperaturforschung

Bayerische Akademie
der Wissenschaften

Spin Fluctuations and Superconductivity in Doped $BaFe_2As_2$

Master's Thesis

Daniel Jost

Advisor: PD Dr. Rudi Hackl
Garching, February 2016

Technische Universität München

Contents

1. Introduction

The experimental and theoretical work on superconductors has come far from its beginnings in 1911, when Heike Kammerlingh Onnes discovered the resistance-free flow of electrons in mercury [1] - a phenomenon nowadays known under the term superconductivity. The most recent discovery of high temperature superconductivity (HTS) in sulfur hydride systems shows once again the potential in this subfield of condensed matter physics [2]. The record for the maximum critical temperature T_c for superconductivity to occur was again broken and stands now at 203 K. In contrast to superconductivity in the cuprates, the ferro-pnictides and most of the other compounds H_3S becomes superconducting only above 90 GPa and reaches the maximum at 190 GPa.

After Onnes' discovery it took nearly half a century to develop a microscopic theory of superconductivity. When Bardeen, Cooper and Schrieffer (BCS) presented their theory in 1957 [3], it had the essential ingredients still effective today. In particular the condensation of the electrons into a bound state called Cooper pairs. However, the BCS theory considered only electron-phonon interaction at the origin of pairing and vanishingly small resistance. The theoretical description of superconductivity was a hallmark of condensed matter theory, and BCS were awarded the Nobel prize in physics in 1972.

In 1986 the quest for higher critical temperatures lead to the discovery of ceramic superconductors by Bednorz and Müller [4], which marked again a scientific break-through. A scientific break-through indeed, as they did not only find a compound with a critical temperature in the regime above 30 K which exceeded the highest critical temperatures in inter metallic compounds. It was not possible to explain the formation of superconductivity in terms of the conventional BCS theory. Especially the phonon "glue" as the pairing mechanism was too weak to explain the formation of Cooper pairs above a temperature of 100 K. Up until today, several mechanisms are debated in order to explain the pairing, such as spin fluctuations or Coulomb and exchange interaction. HTS was found in iron based compounds in 2006 as well [5]. This new zoo of iron based superconductors was quickly extended by the discovery of the iron arsenides

[6] to which the compound $BaFe_2As_2$ belongs. Since then there has been ongoing research, as the origin of superconductivity in these materials has not been pinned down. This is not unlike the situation in the field of the cuprates [7]. Cuprates and iron pnictides show similarities in their physical properties apart from HTS, one of which being magnetic ordering. Both, electron and hole doped $BaFe_2As_2$ samples have regions in the phase diagram, in which superconductivity and magnetic ordering coexist. Additionally a nematic phase and nematic fluctuations have been observed in $Ba(Fe_{1-x}Co_x)_2As_2$ [8]. A sample with $x = 0.051$ was scrutinised in this thesis with respect to its nematic phase and nematic fluctuations. Inelastic light (Raman) scattering is a powerful tool to determine the nature of these fluctuations above the magnetic phase as symmetry selection rules can be applied. The experiments hint towards a scenario which favours spin fluctuations to drive the splitting of the orthorhombic transition at T_s and the magnetic transition at $T_{SDW} < T_s$ as suggested by Fernandes *et al.* [17]. This splitting gives rise to the nematic phase.

Investigating the origin of the magnetic and nematic transitions might lead to a better understanding of the dominating interactions driving superconductivity. The second focus of this thesis laid on the superconducting state in hole doped $Ba_{0.3}K_{0.7}Fe_2As_2$ which showed characteristics indicating a qualitative change of the superconducting gap structure for high hole doping.

This thesis is organised as follows: An overview of the basic properties of the $BaFe_2As_2$ is given in Ch. 2. A short introduction of the Raman effect and Raman spectroscopy is given in Ch. 3 followed by the experimental realisation of a Raman setup in Ch. 4. The experimental results and discussions of the electron doped $Ba(Fe_{0.949}Co_{0.051})_2As_2$ are comprised in Ch. 5. Chapter 6 summarises the results and discussion about the superconducting state in $Ba_{0.3}K_{0.7}Fe_2As_2$.

2. The material class of the iron arsenides

This chapter presents the most basic properties of the iron pnictide $BaFe_2As_2$ and its compounds $Ba(Fe_{1-x}Co_x)_2As_2$ and $Ba_{1-x}K_xFe_2As_2$. Firstly the crystallographic properties is discussed in Sec. 2.1. The phase diagram for cobalt and potassium substitution is presented in Sec. 2.2. Particular focus is laid on the nematic phase in $Ba(Fe_{0.949}Co_{0.051})_2As_2$ in Sec. 2.3 and the superconducting state in $Ba_{0.3}K_{0.7}Fe_2As_2$ in Sec. 2.4.

2.1. Crystallographic properties

The crystal structure of $BaFe_2As_2$ is depicted in Fig. 2.1 (a). The crystal obeys D_{4h} symmetry above any phase transition. The FeAs bonds are stacked between the Ba atoms. The Fe bonds are then again stacked between four As atoms above and one As atom below the Fe plane.
The electronic properties can be attributed to bands composed by the Fe *d*-orbitals. The Ba layers work as spacer layers between these FeAs layers. This is because the spacer layers form bonds of ionic character with the FeAs layer. In contrast the FeAs layers themselves have bonds of covalent (Fe-As) and metallic (Fe-Fe) character in which electrons are "shared" between the atoms [9]. The $\mathbf{k}_z$ dispersion is small and the FeAs plane can be treated as a quasi-2D layer. Due to this confinement one can define the 2 Fe unit cell depicted in Fig. 2.1 (b) with the solid line along the crystal axes a and b. Furthermore, it is convenient to define the 1 Fe unit cell (dashed line) and express the Raman selection rules (see Sec. 3.3) in terms of the axes $\tilde{a}$ and $\tilde{b}$, i. e. along the Fe-Fe bonds. This is physically justified as the *d*-electrons of the Fe dominate the electronic structure.

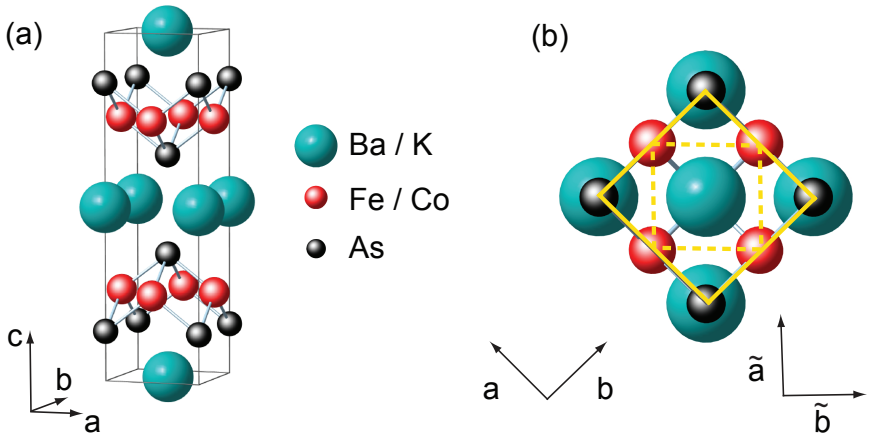

Figure 2.1.: Crystal structure of the tetragonal lattice of $BaFe_2As_2$. (a) Ba atoms (green) stacked above the Fe (red) and As atoms (black). Ba can be substituted by K and Fe by Co. (b) FeAs plane with the axes a and b along the As atoms defining the 2 Fe unit cell (solid line) and the reduced 1 Fe unit cell along the axes $\tilde{a}$ and $\tilde{b}$ (dashed line). Adapted from [10].

The 1 Fe and 2 Fe unit cells are again depicted in Fig. 2.2 (a) as green and dashed black lines. The magnetic unit cell is defined by the solid blue line which is the appropriate unit cell for the spin structure of the SDW phase (see Sec. 2.2). The BZ of the 1 Fe unit cell is shown in (b) along with the Fermi surfaces (FS) of two hole bands around the Γ point and the FS of the electron bands at the X and Y points in red and grey, respectively. The dashed arrow is the folding vector (π, π). The folding vector becomes important, if one takes into account hopping via orbitals of the As. In this case, the As superstructure adds an additional translational symmetry by (π, π). Then, the BZ of the 2 Fe unit cell is half the size of the BZ of the 1 Fe unit cell. The FS of the electron bands at both X and Y point overlap as depicted in the figure. At the intersection points the bands hybridize and exhibit a strong curvature which, in turn, leads to a strong enhancement of the Raman cross section [11].

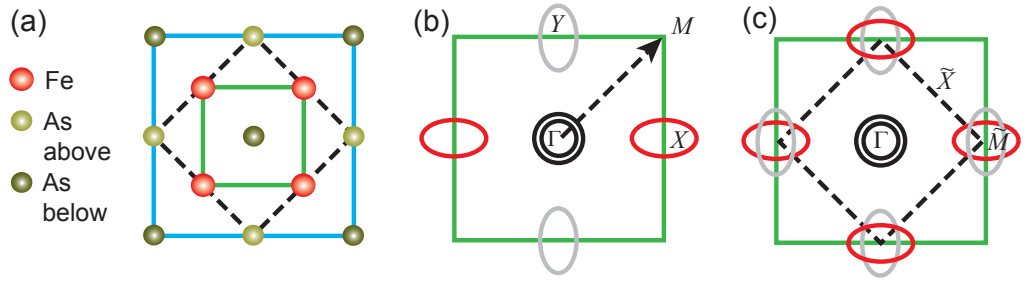

Figure 2.2.: Electronic structure of $BaFe_2As_2$. (a) 2D FeAs plane with the As atoms above an below the Fe-Fe bonds. The green and dashed black line show the 1 and 2 Fe unit cell and the blue line represents the magnetic unit cell. (b) The green line illustrates the 1 Fe BZ with the Fermi surfaces of the hole bands at the Γ point in black and the Fermi surfaces of the electron bands at the X and Y point in red and grey, respectively. (c) Electronic structure after backfolding. The boundaries of the folded BZ are depicted as dashed lines. From [12].

Phonons from vibrations of the As atoms among others are also Raman active. Depicted in Fig. 2.3 are the Raman active phonons in the tetragonal $BaFe_2As_2$. The black arrows indicate the eigenvectors of the phonons. The Ba/K atoms are shown in green. The phonons shown in Fig. 2.2 correspond to the tetragonal unit cell above any phase transition. Symmetry breaking due to phase transitions can yield the appearance of phonons in symmetries other than those depicted. This has been observed for the A_{1g} phonon in $Ba(Fe_{1-x}Co_x)_2As_2$ upon symmetry breaking [12].

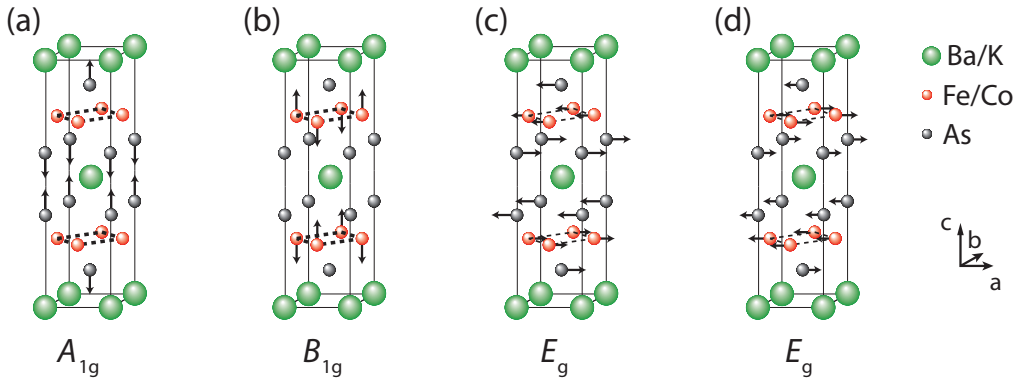

Figure 2.3.: Raman active phonons in $BaFe_2As_2$ type crystals with the black arrows indicating the direction of the lattice vibrations with Ba/K atoms in green, Fe/Co atoms in red and As atoms in grey. From [13].

During the course of this thesis, Raman data were obtained from an electron doped $Ba(Fe_{0.949}Co_{0.051})_2As_2$ sample and a hole doped $Ba_{0.3}K_{0.7}Fe_2As_2$ sample. Doping $BaFe_2As_2$ with K yields an additional hole per 1 Fe unit cell. On the other hand it was suggested [14], that the substitution of Fe with Co should not be considered as carrier doping in the "conventional" meaning of the word (see Sec. 2.2 for more details). Nevertheless both, K and Co substitution, yield an interesting phase diagram.

2.2. Phase diagram and transitions in doped $BaFe_2As_2$

In Fig. 2.4 the phase diagram of $BaFe_2As_2$ is depicted with the control parameter doping x (here: potassium and cobalt substitution). The regions of the phase diagram which are important for the discussion of the results are outlined in the following.

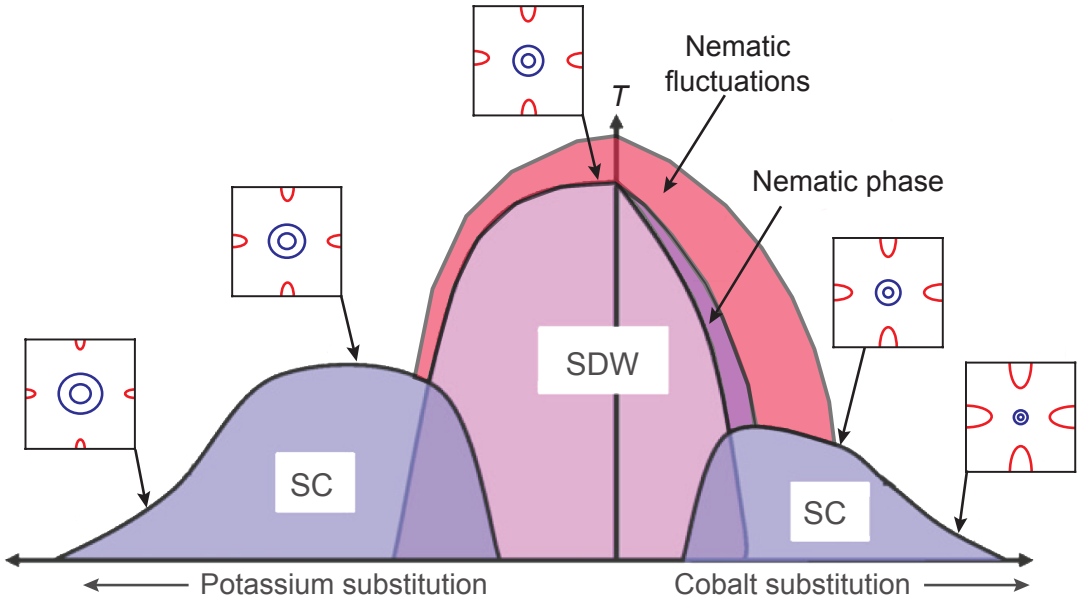

Figure 2.4.: Generic phase diagram of the $BaFe_2As_2$ for hole and electron doped samples. The range in which nematic fluctuations are observed is depicted in red [15], the nematic phase in violet. Both sides of the phase diagram show a superconducting dome in blue. Additionally, the band structure in the BZ is depicted for several doping levels on both sides of the diagram with hole bands in blue and electron bands in red. Adapted from [16] and [17]. Modifications from [12].

For zero doping, $BaFe_2As_2$ exhibits nematic fluctuations setting in at a temperature T_f before entering the structural transition at T_s. At T_s the tetragonal lattice is orthorhombically distorted meaning that the crystallographic axes are not orthogonal any further. The lengths of the orthorhombic axes differ by 0.7 % leading to twinning effects which manifest themselves as stripes on the sample's surface. The observation of these stripes proved to be a reliable probe in the determination of T_s [18]. The structural transition temperature T_s coincides with a magnetic ordering temperature T_{SDW}. Magnetic ordering means the development of a stripe-like Spin-Density-Wave (SDW) which is anisotropic with respect to the magnetic axes $\tilde{a}$, $\tilde{b}$. Hence, one finds ferromagnetic or parallel spin ordering along $\tilde{b}$ and antiferromagnetic or antiparallel spin ordering along $\tilde{a}$.
Substitution of Fe with Co in $Ba(Fe_{1-x}Co_x)_2As_2$ yields superconductivity setting in at $x = 0.025$. The critical temperature T_c increases up to a maximum of $T_c = 26$ K with an

optimal doping concentration $x = 0.062$. Co substitution yields shrinking of the hole bands at the Γ point as indicated qualitatively in Fig. 2.4. The electrons at the X and Y point expand [19]. Wadati *et al.* suggested [14], that the substitution of Fe with Co does not add electrons to the unit cell. Rather, the excess electrons coming from the Co stay close to substitute site to compensate for the nuclear charge. The occurrence of superconductivity can then be explained in terms of impurity scattering. As the substitution still takes place in the quasi 2D FeAs plane, the Co impurities would act as strong scatterers in this scenario which "wash out" the Fermi surface. Particularly the regions with small Fermi velocity (i. e. the flat band contributions) would be washed out first. This could destabilise the SDW ordering in favour of superconductivity. This picture does not affect the interpretation of the data presented in this thesis. Co substitution is further referred to as electron doping.
Hole doping with potassium reduces the size of the electron bands at the X and Y points and expands the hole bands at the Γ point. The electron bands disappear entirely for a doping $x \approx 0.8$ [20]. Superconductivity sets in at $x = 0.22$ and reaches a maximal $T_c = 39$ K at $x = 0.4$. If Ba is completely replaced by K ($x = 1$) superconductivity with $T_c = 4$ K survives. The change in topology of both electron and hole bands has not been entirely clarified yet. ARPES measurements and Raman data obtained for the $Ba_{0.3}K_{0.7}Fe_2As_2$ are consistent with a Lifshitz transition of the electron bands in a doping interval $0.6 < x < 0.8$ (see Ch. 6).

2.3. Nematicity and magnetic ordering in $Ba(Fe_{1-x}Co_x)_2As_2$

The nematic phase is known for its occurrence in nematic liquid crystals some of which are used in Liquid Crystal Displays (LCDs). Fig. 2.5 illustrates the concept of a liquid crystal (LC). In (a) the molecules of an LC are drawn above the nematic ordering temperature T_{nem} in its isotropic phase. The molecules itself are anisotropic. Upon cooling below T_{nem} the molecules exhibit local ordering along a so called director $\mathbf{n}$. This local ordering breaks the rotational invariance, but does not lead to a long-range translational order.

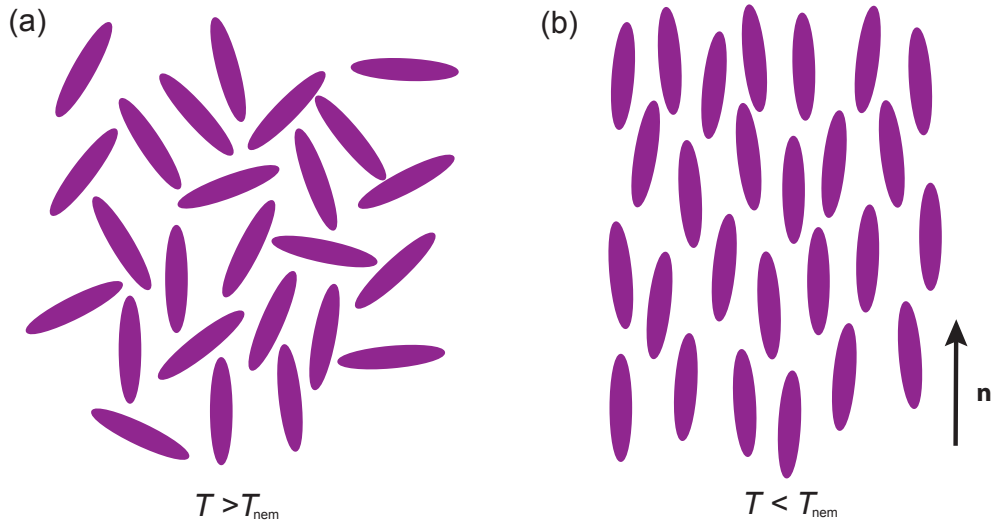

Figure 2.5.: Liquid crystal. (a) Anisotropic molecules in the isotropic phase at $T > T_{\text{nem}}$. (b) Local order is established with the average orientation along the director $\mathbf{n}$ at $T < T_{\text{nem}}$.

One might draw the analogy of electronic fluids to be quantum versions of a liquid crystal. The terms electronic nematicity or electronic nematic order are used to describe a phase in which an electron fluid breaks a symmetry of the underlying system. In spite of the controversial discussion about its origin, it is a widely accepted fact, that electronic nematic order also exists in iron arsenides, and particularly in $Ba(Fe_{1-x}Co_x)_2As_2$. Here, the orthorhombic distortion is not caused by phonons or lattice degrees of freedom, but rather by electronic degrees of freedom [21, 22]. The electron fluid breaks the C_4 symmetry while preserving the $O(3)$ spin rotational (or time reversal) symmetry. The $O(3)$ spin rotational symmetry is broken upon magnetic ordering below T_{SDW}. Then, the time average over a magnetic moment on every lattice site does not vanish any further.

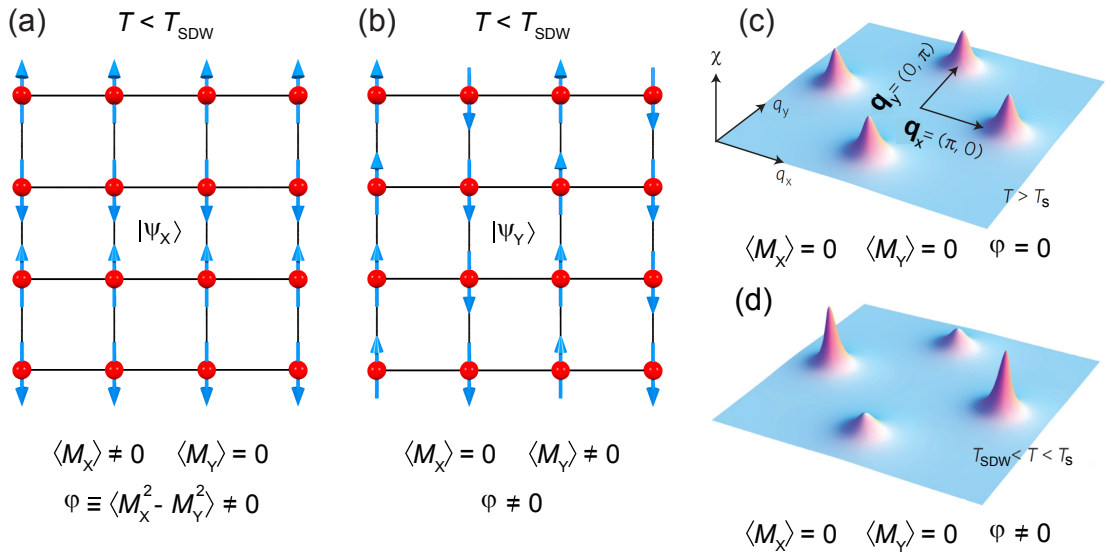

Figure 2.6.: The two degenerate magnetic ground states $|\psi_x\rangle$ in (a) and $|\psi_y\rangle$ in (b) with the Fe atoms in red. Magnetic moments are illustrated as blue arrows. (c) For temperatures $T >> T_s$ the susceptibility near the ordering vectors $\mathbf{q}_x$ and $\mathbf{q}_y$ is equally strong within each BZ and $\langle M_X^2 \rangle = \langle M_Y^2 \rangle$. (d) Upon cooling through T_s the susceptibility increases along one ordering vector of this state and $\varphi \neq 0$. From [12] and [17].

Similar to the director in liquid crystals, an order parameter $\varphi = \langle M_X^2 - M_Y^2 \rangle$ for the nematic phase can be found. This order parameter is motivated by the configuration of the ground states in the SDW phase $|\psi_x\rangle$ and $|\psi_y\rangle$. To these ground states correspond magnetic ordering vectors $\mathbf{q}_x = (\pi, 0)$ and $\mathbf{q}_y = (0, \pi)$ in the BZ of the 1 Fe unit cell. Furthermore, one can introduce magnetic order parameters M_X and M_Y with their averages being $\langle M_X \rangle$, $\langle M_Y \rangle$. One may think of these order parameters as magnetisations in momentum space. Their averages become finite for parallel spin alignment and are zero for anti-parallel spin alignment. Fig. 2.6 shows (a) the configuration in the ground state $|\psi_x\rangle$ and (b) in the ground state $|\psi_y\rangle$ below T_{SDW}. In the ground state $|\psi_x\rangle$ parallel spin alignment along X and anti-parallel spin alignment along Y leads to $\langle M_X \rangle \neq 0$ and $\langle M_Y \rangle = 0$ and vice versa for the ground state $|\psi_y\rangle$. The nematic order parameter is finite and thus both, C_4 and $O(3)$ symmetries are broken. The scenario far above T_s is depicted in (c). The susceptibility χ along $\mathbf{q}_x$ and $\mathbf{q}_y$ is equally strong and the nematic order parameter φ is zero. In the nematic phase $T_{SDW} < T < T_s$ (cf. Fig. 2.6 (d)) the susceptibility along the ordering vectors $\mathbf{q}_x$ and $\mathbf{q}_y$ is not equal any further.

This breaks the C_4 symmetry. The nematic order parameter φ becomes finite, whereas the time average over the magnetic moment on every lattice site still vanishes. This preserves the $O(3)$ spin rotational symmetry.
A mean-field approach predicts a breaking of both C_4 and $O(3)$ symmetries simultaneously at the magnetic transition T_{SDW}. In terms of the magnetic susceptibility one can write [23]

$$\chi_{mag}(\mathbf{q}) = \frac{1}{T - T_{SDW} + (\mathbf{q} - \mathbf{q}_c)^2} \tag{2.1}$$

in which $\mathbf{q}_c$ is the ordering or critical wave vector. In accordance with the illustration above this is $\mathbf{q}_c = \mathbf{q}_x, \mathbf{q}_y$. For $\mathbf{q} = \mathbf{q}_c$ Eqn. 2.1 diverges at T_{SDW}. However, if one includes fluctuations of the nematic order parameter φ the nematic susceptibility is given via [17]

$$\chi_{nem} = \frac{\int_{\mathbf{q}} \chi^2_{mag}(\mathbf{q})}{1 - g \int_{\mathbf{q}} \chi^2_{mag}(\mathbf{q})} \tag{2.2}$$

with the nematic coupling constant g. Eqn. 2.2 diverges at a temperature $T^* > T_{SDW}$. This consideration of fluctuations splits the transitions. Hence, the breaking of C_4 and $O(3)$ symmetry are split which gives rise to an intermediate phase. In this phase the C_4 symmetry is broken and the $O(3)$ symmetry is preserved which is the definition of a nematic phase. This phase is driven by fluctuations of unequal strength along $\mathbf{q}_x$ and $\mathbf{q}_y$. In Sec. 5.4 fluctuations along $\mathbf{q}_x$ and $\mathbf{q}_y$ are discussed to be the driving force behind nematic order in $Ba(Fe_{0.949}Co_{0.051})_2As_2$.
$Ba(Fe_{0.949}Co_{0.051})_2As_2$ also exhibits superconductivity. Although the fluctuations disappear upon magnetic ordering, the coexistence of superconductivity and SDW phase might indicate a connection between spin fluctuations and the emergence of superconductivity.
The superconducting ground state in $BaFe_2As_2$ compounds exhibits interesting phenomena as well. The next section gives a short overview of superconductivity with respect to the discussion following the results of $Ba_{0.3}K_{0.7}Fe_2As_2$ in Ch. 6.

2.4. Superconductivity and the collective mode in $Ba_{0.3}K_{0.7}Fe_2As_2$

Superconductivity emerges from quantum coherence and the formation of electron pairs - so called Cooper pairs - below a critical temperature T_c.
Cooper showed, that two electrons placed in a shell with width $\hbar\omega_0$ (cf. Fig. 2.8 (a)) around a fully occupied Fermi surface would form a bound state in the presence of a

weak attracting interaction. Together with Bardeen and Schrieffer, he developed the first microscopic theory of superconductivity [3].
Fig. 2.7 depicts a Feynman diagram illustrating an electron-electron interaction. The interaction is mediated via an exchange boson. In the BCS theory, this exchange boson is a phonon for conventional superconductors, the maximum frequency of which is given by the Debye frequency ω_D. The phonon transports the momentum $\mathbf{q}$ from electron 1 to electron 2.

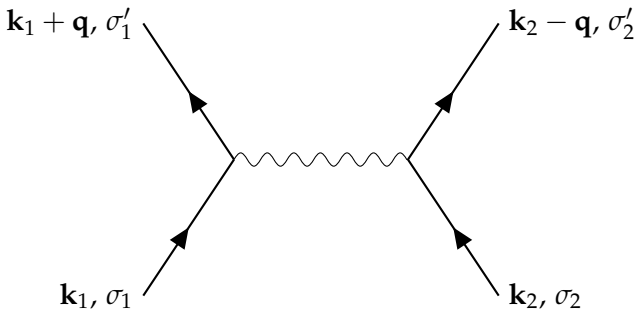

Figure 2.7.: Fermion interaction. Two electrons in states with initial momenta $\mathbf{k}_1$, $\mathbf{k}_2$ and spins σ_1, σ_2 interact via an exchange boson represented by the wavy line.

The spin configurations of the Cooper pair are given as in any two-fermion system. The two possible configurations are either a singlet state with total spin $S = 0$ or a triplet state with $S = 1$. If one considers a very rudimentary approach to the wave function of such Cooper pairs, one can write it in terms of a spatial part $|\phi(\mathbf{r})\rangle$ and a spin part $|\sigma(\mathbf{s})\rangle$:

$$|\Psi(\mathbf{r}, \mathbf{s})\rangle \propto |\phi(\mathbf{r})\rangle \cdot |\sigma(\mathbf{s})\rangle \tag{2.3}$$

A two-fermion wave function has to be antisymmetric. Thus, for the antisymmetric singlet state, the spatial part needs to be symmetric and vice versa for the triplet state. The pairing states are called either s, d, g,... states for $S = 0$ or p, f, h,... states for $S = 1$ in analogy to atomic orbitals. The BCS wave function is also the order parameter in the superconducting state.
In the bound state, the electrons reduce their energy by a factor of $\Delta_{\mathbf{k}}(T)$ relative to the Fermi energy. This is given by the expression of the BCS gap equation [24]

$$\Delta_{\mathbf{k}}(T) = -\sum_{\mathbf{k}'} \frac{V_{\mathbf{k},\mathbf{k}'} \cdot \Delta_{\mathbf{k}'}}{2E_{\mathbf{k}'}} \tanh(E_{\mathbf{k}'}/k_B T) \tag{2.4}$$

with the BCS interaction potential $V_{\mathbf{k},\mathbf{k}'}$ and the band energy $E_{\mathbf{k}'}$. $V_{\mathbf{k},\mathbf{k}'}$ represents the

potential which is effective over the entire Fermi surface. BCS assumed an isotropic potential $V_{\mathbf{k},\mathbf{k}'} = -V_0$ in order to solve the gap equation. They found the ground state to be of singlet s-wave symmetry in convenctional superconductors. Other symmtries were found for unconventional superconductors such as d-wave paring in cuprates and more exotic configurations are discussed such as $s + id$ coupling in iron pnictides [25].

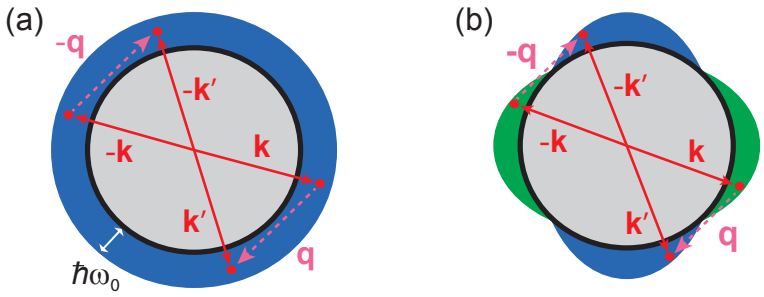

Figure 2.8.: Pair scattering process of two electrons in (a) an isotropic potential and (b) an anisotropic potential by scattering vectors $\mathbf{q}$ and $-\mathbf{q}$. See text for details. From [12].

Schematically depicted in Fig. 2.8 are two scenarios for the pairing potential. In (a) an isotropic potential is depicted. An electron pair $\mathbf{k}, -\mathbf{k}$ is scattered into $\mathbf{k}', -\mathbf{k}'$ by two bosons with momenta $\mathbf{q}$ and $-\mathbf{q}$. The same is seen in (b), yet here the interaction potential is firstly anisotropic and secondly the scattering mechanism requires a sign change of the order parameter. Both have in common, that the scattering occurs at one Fermi surface. They depict *intra band* scattering.

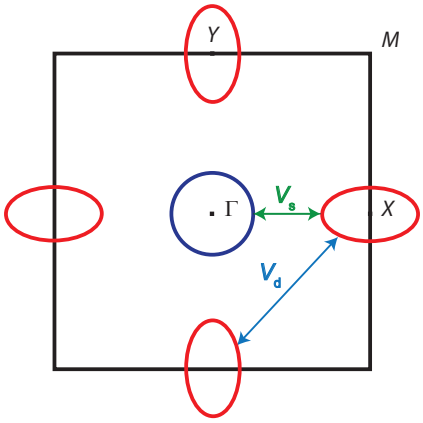

Figure 2.9.: Inter band pairing in $Ba_{1-x}K_xFe_2As_2$ in the BZ of the 1 Fe unit cell, along with the dominant *s*-wave pairing and subdominant *d*-wave pairing with pairing potentials V_s and V_d. Blue indicates the hole band at the Γ point and red the slightly elliptic electron bands at the *X* and *Y* point.

However, in the superconducting $Ba_{1-x}K_xFe_2As_2$, the pairing mechanism is believed to be of *s*-wave *inter band* scattering between the hole and electron bands in the BZ of the 1 Fe unit cell for doping concentrations around optimal doping [26]. An illustration is shown in Fig. 2.9 with the two pairing potentials V_s and V_d. The dominant *s*-pairing channel corresponds to the potential V_s. Due to the occurrence of the subdominant *d*-channel corresponding to V_d, modes emerge in the Raman spectra of $Ba_{0.3}K_{0.7}Fe_2As_2$, as shall be seen in Ch. 6. The occurrence of these modes might give further insight into the underlying mechanisms which give rise to superconductivity.
Raman spectroscopy has proven to be an excellent probe to investigate such behaviour of the novel iron pnictides. The distinct advantages of Raman spectroscopy will be discussed in the following chapter.

3. Theory of Raman scattering

As a colleague and friend put it quite poetically, Raman spectroscopy is as if one hits an object with a hammer and listens to the sound of matter.
In a less poetic way, this chapter shall first and foremost give an overview of the theoretical construct which is necessary to perform Raman spectroscopy. An in-depth discussion can be found in the Review of Modern Physics by Devereaux and Hackl [27].
After the presentation of the basic principles in Sec. 3.1 a summary of the most important theoretical pieces of the underlying photon-electron interaction is given in Sec. 3.2. The chapter closes with an illustration of the symmetry arguments and the selection rules which make Raman spectroscopy such a powerful tool for understanding correlated electron systems.

3.1. Basic principle of electronic Raman scattering

The basic concept of the Raman process is a consequence of the conservation of energy and momentum. Suppose an electron in an initial state $|\mathrm{i}\rangle$ in a solid state system. A photon with energy ω_i and momentum $\mathbf{k}_\mathrm{i}$ can excite this electron into a virtual state $|\nu\rangle$. Virtual state means that the lifetime of the state is shorter than the limit given by Heisenberg's uncertainty relation. The vast majority of the electrons scatters elastically or in other words, scatters back into the initial state $|\mathrm{i}\rangle$. However, every 10^{13}th electron will relax into a final state $|\mathrm{f}\rangle \neq |\mathrm{i}\rangle$ emitting a photon with frequency $\omega_\mathrm{s} \neq \omega_\mathrm{i}$ and momentum $\mathbf{k}_\mathrm{s} \neq \mathbf{k}_\mathrm{i}$. The conservation laws

$$\mathbf{q} = \mathbf{k}_\mathrm{i} \pm \mathbf{k}_\mathrm{s} \tag{3.1}$$

$$\Omega = \omega_\mathrm{i} \pm \omega_\mathrm{s} \tag{3.2}$$

require, that the energy Ω and momentum $\mathbf{q}$ must either remain in the system in form of an excitation if $\mathbf{k}_\mathrm{i} > \mathbf{k}_\mathrm{s}$ or an excitation $(\Omega, \mathbf{q})$ must be destroyed for the case $\mathbf{k}_\mathrm{i} < \mathbf{k}_\mathrm{s}$. The energy Ω is called the Raman shift. There are various excitations in solid state systems apart from the electron (rather electron-hole) excitations used in the example.

Among these are phonons, magnons and polarons not all of which are Raman active. The process creating an excitation is called the Stokes process. The destruction of an excitation is called the Anti-Stokes process. Schematically depicted are both processes in Fig. 3.1.

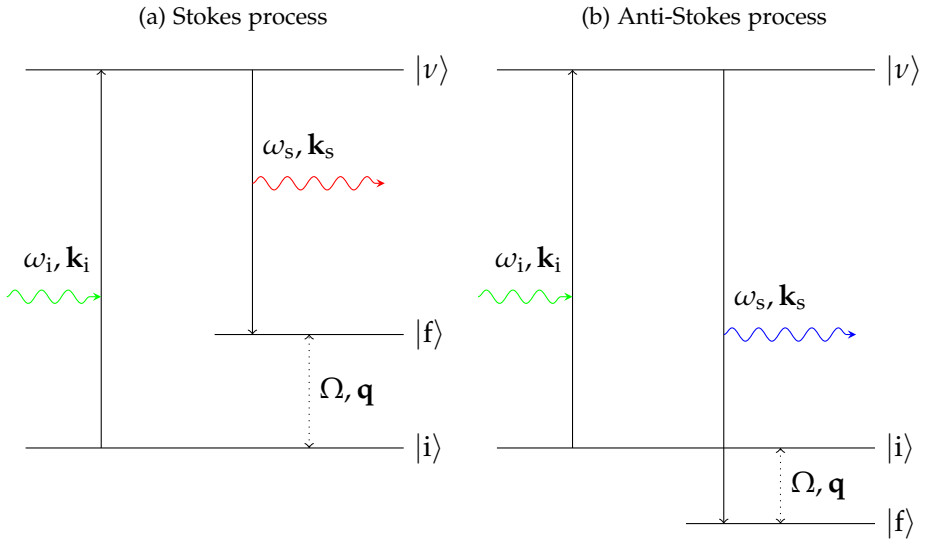

Figure 3.1.: Raman scattering processes: a photon with energy ω_i and momentum $\mathbf{k}_i$ excites an electron in the initial state $|i\rangle$ into a virtual state $|\nu\rangle$. As this short-lived state decays relaxation of the electron into a final state $|f\rangle \neq |i\rangle$ takes place and a photon is emitted with ω_s, $\mathbf{k}_s$. An excitation of the system with an energy Ω and a momentum $\mathbf{q}$ is either (a) created during the Stokes process or (b) destroyed during the Anti-Stokes process. From [28].

Both processes have in common the occurrence of two dipole transitions.

3.2. Scattering cross section and photon-electron coupling

An experimental setup as described in Ch. 4 can harvest the photons emitted during the second dipole transition. The number of photons is counted which scatter in an angle interval $[\Omega, \Omega + d\Omega]$ and a frequency window $[\omega_s, \omega_s + d\omega_s]$ for a given time period. The rate of photons $\dot{N}(\Omega, T)$ with frequency ω_s is plotted against the Raman

shift Ω. This rate is proportional to the differential scattering cross angle

$$\dot{N}(\omega, T) \propto \frac{\partial^2 \sigma}{\partial \Omega \partial \omega_s} = \hbar r_0^2 \frac{\omega_s}{\omega_i} \mathcal{R} \tag{3.3}$$

with the Thomson radius $r_0 = e^2/4\pi\epsilon_0 mc^2$ and the transition rate $\mathcal{R}$. The selection of different polarisations for the incoming and scattering photons yields the resolution of different parts of the Brillouin zone (BZ).

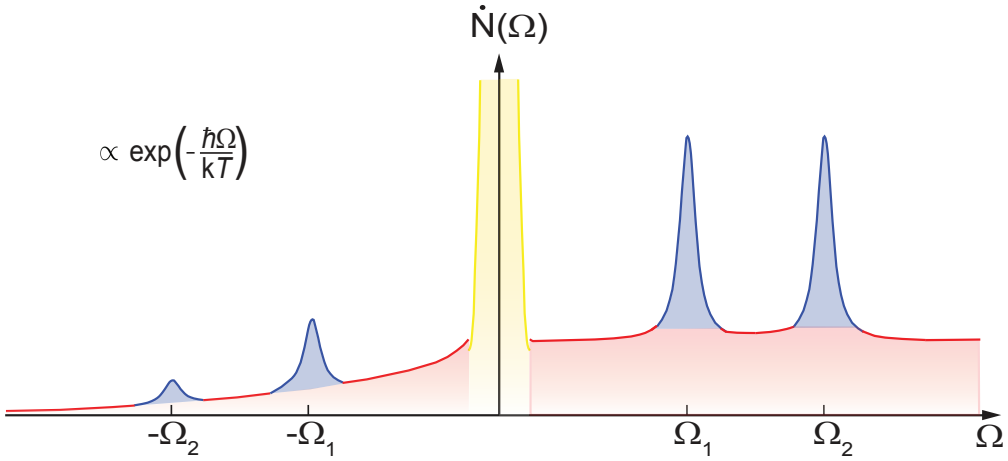

Figure 3.2.: Scheme of a Raman spectrum with contributions from electron-hole excitations in red and phonons in blue. Plotted in yellow is the contribution from elastically scattered photons at $\Omega = 0$. The negative Ω values correspond to contributions from the Anti-Stokes-process. The positive values result from the Stokes-process. From [12].

Fig. 3.2 shows a schematic spectrum with contributions from electron-hole excitations (particle-hole or p-h continuum) and phonons in blue which sit on top of it. The negative Ω values correspond to contributions from the Anti-Stokes-process. The positive values result from the Stokes-process. For the rates $\dot{N}_{\text{Stokes}}$ and $\dot{N}_{\text{Anti-Stokes}}$ the relation

$$\frac{\dot{N}_{\text{Anti-Stokes}}}{\dot{N}_{\text{Stokes}}} = \exp\left[-\frac{\hbar\Omega}{k_B T}\right] \tag{3.4}$$

holds. In the region of $\Omega = 0$ elastically scattered photons yield a peak shown in yellow. The majority of electrons scattered into a virtual state $|\nu\rangle$ relaxes into the initial state $|i\rangle$.

The signal for zero Raman shift $\Omega = 0$ is strongly enhanced. The width of this so called central line is dependent on the resolution of the spectrometer and is superposed on the spectrum resulting from the inelastically scattered photons with small Raman shift $\Omega \approx 0$.
Eqn. 3.3 shall be simplified in the following to find an expression for the experimental quantity $\dot{N}(\Omega, T)$. $\dot{N}$ will be connected to the imaginary part of the Raman response function [1]. For this the transition rate $\mathcal{R}$ is simplified to a correlation function. Firstly it is given by Fermi's Golden Rule and reads

$$\mathcal{R} = \frac{1}{\mathcal{Z}} \sum_{i,f} \exp\left[-\beta E_i\right] |\mathcal{M}_{f,i}|^2 \delta(E_f - E_i - \hbar\Omega) \tag{3.5}$$

with the partition function $\mathcal{Z}$ and $\beta = 1/k_B T$. $\mathcal{M}_{f,i}$ is the matrix element $\mathcal{M}_{f,i} = \langle f| \hat{\mathcal{M}} |i\rangle$ in which $\hat{\mathcal{M}}$ is the transition operator.
The matrix element $\mathcal{M}_{f,i}$ is determined by the Hamiltonian of N electrons interacting with an electromagnetic field

$$\hat{\mathcal{H}} = \hat{\mathcal{H}}_{\text{Coulomb}} + \hat{\mathcal{H}}_{\text{fields}} + \sum_i^N \frac{\left[\hat{\mathbf{p}}_i + (e/c)\hat{\mathbf{A}}(\mathbf{r}_i)\right]^2}{2m} \tag{3.6}$$

with the electron charge e, the electron mass m, the momentum operator $\hat{\mathbf{p}}$ and the vector potential operator $\hat{\mathbf{A}}(\mathbf{r}_i)$. $\hat{\mathcal{H}}_{\text{fields}}$ is the contribution of the free electromagnetic field and $\hat{\mathcal{H}}_{\text{Coulomb}}$ the Coulomb interaction term. Expansion and reposition of Eqn. 3.6 yields

$$\hat{\mathcal{H}} = \hat{\mathcal{H}}' + \frac{e}{2mc} \sum_i^N \left[\hat{\mathbf{p}}_i \cdot \hat{\mathbf{A}}(\mathbf{r}_i) + \hat{\mathbf{A}}(\mathbf{r}_i) \cdot \hat{\mathbf{p}}_i\right] + \frac{e^2}{2mc^2} \sum_i^N \hat{\mathbf{A}}(\mathbf{r}_i) \cdot \hat{\mathbf{A}}(\mathbf{r}_i). \tag{3.7}$$

The non-interacting Hamiltonian $\hat{\mathcal{H}}' = \hat{\mathcal{H}}_0 + \hat{\mathcal{H}}_{\text{fields}}$ with $\hat{\mathcal{H}}_0 = {}^1/_{2m} \sum_i \hat{\mathbf{p}}_i^2 + \hat{\mathcal{H}}_{\text{Coulomb}}$ is the standard Hamiltonian of particles in a Coulomb field. $\hat{\mathcal{H}}'$ does not have a contribution to the photon-electron interaction; thus, the relevant interaction Hamiltonian is reduced to

$$\hat{\mathcal{H}}_{\text{int}} = \frac{e}{2mc} \sum_i^N \left[\hat{\mathbf{p}}_i \cdot \hat{\mathbf{A}}(\mathbf{r}_i) + \hat{\mathbf{A}}(\mathbf{r}_i) \cdot \hat{\mathbf{p}}_i\right] + \frac{e^2}{2mc^2} \sum_i^N \hat{\mathbf{A}}(\mathbf{r}_i) \cdot \hat{\mathbf{A}}(\mathbf{r}_i). \tag{3.8}$$

The first sum describes the coupling of the electron's momentum to one single photon and the second term describes the coupling of the electron's charge to two photons. With some effort, one can extract an expression for the matrix element from this

[1] A response function can be written as $\chi = \chi' + i\chi''$ with real part χ' and imginary part χ''.

Hamiltonian which can be found elsewhere [27]. Then, Eqn. 3.5 can be simplified to a correlation function $\tilde{S}(\mathbf{q}, i\Omega)$ and the scattering cross section reads

$$\frac{\partial^2\sigma}{\partial\Omega\partial\omega_\mathrm{s}} = \hbar r_0^2 \frac{\omega_\mathrm{s}}{\omega_\mathrm{i}} \tilde{S}(\mathbf{q},\ i\Omega \to \Omega + i0) \tag{3.9}$$

with the correlation function

$$\tilde{S}(\mathbf{q},\ i\Omega) = \sum_\mathrm{i} \frac{\exp\left[-\beta E_\mathrm{i}\right]}{\mathcal{Z}} \int \mathrm{d}\tau \exp[i\Omega\tau] \left\langle \mathrm{i}\right| T_\tau \rho(\mathbf{q},\tau)\rho(-\mathbf{q},0) \left|\mathrm{i}\right\rangle . \tag{3.10}$$

T_τ is the time ordering operator, and the effective density operator reads

$$\rho(\mathbf{q}) = \sum_{\mathbf{k},\sigma} \gamma(\mathbf{k},\mathbf{q}) c^\dagger_{\mathbf{k}+\mathbf{q},\sigma'}\ c_{\mathbf{k},\sigma} \tag{3.11}$$

with creation operator $c^\dagger_{\mathbf{k}+\mathbf{q},\sigma'}$ and annihilation operator $c_{\mathbf{k},\sigma}$. The process describes the scattering of an electron with momentum $\mathbf{k}$ and spin σ into a state with momentum $\mathbf{k}+\mathbf{q}$ and spin σ'. This scattering process is "weighted" by the scattering amplitude $\gamma(\mathbf{k},\mathbf{q})$ which is given by

$$\gamma(\mathbf{k},\mathbf{q}) = \sum_{\alpha,\beta} \gamma_{\alpha,\beta}(\mathbf{k},\mathbf{q}) e^\alpha_\mathrm{i} e^\beta_\mathrm{s}. \tag{3.12}$$

$\gamma_{\alpha,\beta}(\mathbf{k},\mathbf{q})$ are the Raman matrix elements and e^α_i and e^β_s incident and scattering vectors. Applying the fluctuation-dissipation theorem [29] $\tilde{S}(\mathbf{q},\Omega)$ can be written in terms of the imaginary part $\chi''(\mathbf{q},\Omega)$ of the Raman response $\chi(\mathbf{q},\Omega)$:

$$\tilde{S}(\mathbf{q},\Omega) = -\frac{1}{\pi}\left[1 + n(\Omega,T)\right] \cdot \chi''(\mathbf{q},\Omega) \tag{3.13}$$

$n(\Omega,T)$ is the Bose-Einstein distribution function. Finally, we arrive at an expression for $\dot{N}(\Omega,T)$ which is directly connected to the Raman response function $\chi(\mathbf{q},\Omega)$:

$$\dot{N}(\Omega,T) = R \cdot \left[1 + n(\Omega,T)\right] \cdot \chi''(\mathbf{q},\Omega) \tag{3.14}$$

All components which are neither temperature nor frequency dependent are included in the scale factor R.

3.3. Symmetry and selection rules

The Raman matrix in Eqn. 3.12 can be simplified. With $\mathbf{q} \to 0$ and the effective mass approximation [30] one can write

$$\gamma_{\alpha,\beta}(\mathbf{k},\mathbf{q}\to 0) = \frac{1}{\hbar^2}\frac{\partial^2\epsilon_\mathbf{k}}{\partial k_\alpha \partial k_\beta} = \frac{1}{m_\mathrm{eff}} \tag{3.15}$$

with the energy dispersion $\epsilon_{\mathbf{k}}$. In a 2D-system this reads:

$$\gamma_{x,y}(\mathbf{k}, \mathbf{q} \to 0) = \frac{1}{m_{\text{eff}}} = \frac{1}{\hbar^2} \begin{bmatrix} \frac{\partial^2 \epsilon_{\mathbf{k}}}{\partial k_x^2} & \frac{\partial^2 \epsilon_{\mathbf{k}}}{\partial k_x \partial k_y} \\ \frac{\partial^2 \epsilon_{\mathbf{k}}}{\partial k_y \partial k_x} & \frac{\partial \epsilon_{\mathbf{k}}^2}{\partial k_y^2} \end{bmatrix} \tag{3.16}$$

The tensor describes the curvature of the bands in the two dimensional $\mathbf{k}$ space. This curvature is positive for hole-like bands and negative for electron-like bands. With this, the scattering amplitude or Raman vertex from Eqn. 3.12 is given by

$$\gamma(\mathbf{k}) = \mathbf{e}_{\text{s}}^* \; m_{\text{eff}}^{-1} \; \mathbf{e}_{\text{i}}. \tag{3.17}$$

The vectors $\mathbf{e}_{\text{s}}^*$ and $\mathbf{e}_{\text{i}}$ are again the polarisation vectors of the scattering and the incident light, respectively. These vectors are written out in Tab. 3.1. The x axis points along $\tilde{b}$ and the y axis along $\tilde{a}$. x' and y' are rotated by an angle of 45°. R and L denote right-handed and left-handed circular light (cf. Fig. 3.4).

Table 3.1.: Polarisation vectors.

Polarisation	x	y	x'	y'	R	L
Vectors	$\begin{pmatrix} 1 \\ 0 \end{pmatrix}$	$\begin{pmatrix} 0 \\ 1 \end{pmatrix}$	$\frac{1}{\sqrt{2}}\begin{pmatrix} 1 \\ 1 \end{pmatrix}$	$\frac{1}{\sqrt{2}}\begin{pmatrix} -1 \\ 1 \end{pmatrix}$	$\frac{1}{\sqrt{2}}\begin{pmatrix} 1 \\ i \end{pmatrix}$	$\frac{1}{\sqrt{2}}\begin{pmatrix} 1 \\ -i \end{pmatrix}$

If $\epsilon_{\mathbf{k}}$ is known, one can calculate the contributions from different Fermi sheets in the BZ. But even without the exact knowledge of the band structure, symmetry arguments apply. The matrix element can be decomposed in the $\mathbf{q} \to 0$ limit [27]

$$\mathcal{M}_{\text{f,i}}(\mathbf{q} \to 0) = \sum_{\mu} \mathcal{M}_{\mu} \Phi_{\mu}. \tag{3.18}$$

Φ_{μ} are the basis functions or crystal harmonics of the irreducible point group with the representation of such a group μ. The decomposition for the $D_{4\text{h}}$ point group reads

$$\begin{aligned} \mathcal{M}_{\text{f,i}} = &\frac{1}{2}\hat{\mathcal{O}}_{A_{1\text{g}}^{(1)}} \left(e_{\text{i}}^x e_{\text{f}}^x + e_{\text{i}}^y e_{\text{f}}^y\right) + \frac{1}{2}\hat{\mathcal{O}}_{A_{1\text{g}}^{(2)}} \left(e_{\text{i}}^z e_{\text{f}}^z\right) \\ &+\frac{1}{2}\hat{\mathcal{O}}_{B_{1\text{g}}} \left(e_{\text{i}}^x e_{\text{f}}^x - e_{\text{i}}^y e_{\text{f}}^y\right) + \frac{1}{2}\hat{\mathcal{O}}_{B_{2\text{g}}} \left(e_{\text{i}}^x e_{\text{f}}^y - e_{\text{i}}^y e_{\text{f}}^x\right) \\ &+\frac{1}{2}\hat{\mathcal{O}}_{A_{2\text{g}}} \left(e_{\text{i}}^x e_{\text{f}}^y - e_{\text{i}}^y e_{\text{f}}^x\right) + \frac{1}{2}\hat{\mathcal{O}}_{E_{\text{g}}^{(1)}} \left(e_{\text{i}}^x e_{\text{f}}^z + e_{\text{i}}^z e_{\text{f}}^x\right) \\ &+\frac{1}{2}\hat{\mathcal{O}}_{E_{\text{g}}^{(2)}} \left(e_{\text{i}}^y e_{\text{f}}^z + e_{\text{i}}^z e_{\text{f}}^y\right) \end{aligned} \tag{3.19}$$

with projection operators $\hat{\mathcal{O}}_\mu$. The choice of the polarisations of the incoming and outgoing light determines which elements of the point group are projected out [2].

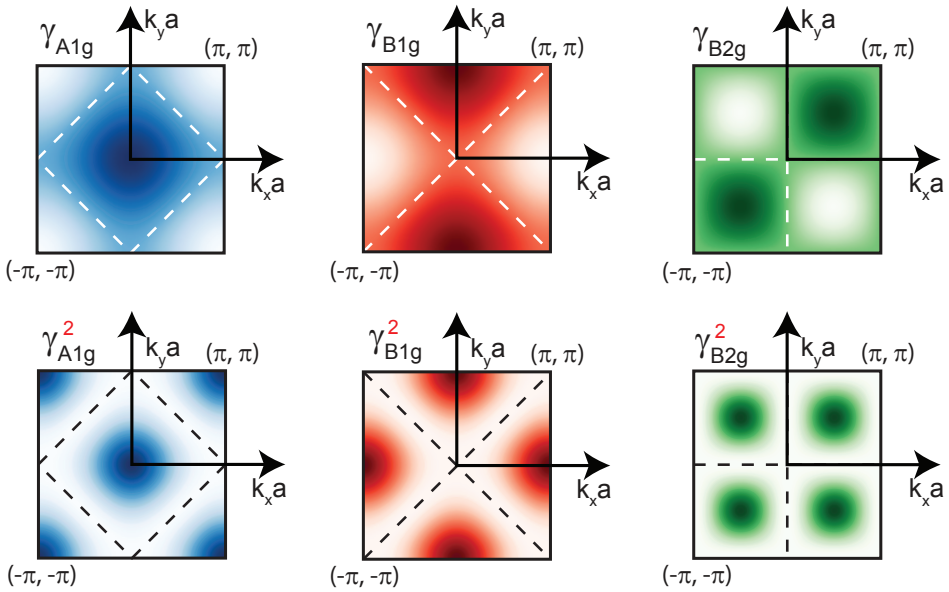

Figure 3.3.: The Raman vertices γ_μ are depicted for $\mu = A_{1g}, B_{1g}, B_{2g}$ in the first row. The second row shows the squares of the Raman vertices γ_μ^2. Dashed lines show the nodes where γ_μ vanishes. From [32].

The Raman vertex γ_μ and the square of it γ_μ^2 are depicted for the symmetries $\mu = A_{1g}, B_{1g}, B_{2g}$ in Fig. 3.3. The colouration indicates the areas of the BZ which can be projected out by choice of the corresponding incident and scattering vectors. This illustrates the advantage of Raman spectroscopy over some other spectroscopy methods, for instance IR spectroscopy which gains the average over the entire BZ.

Table 3.2.: Polarisations of the incoming and scattering light and the contributions from A_{1g}, A_{2g}, B_{1g} and B_{2g} symmetries.

$xx(yy)$	$x'x'(y'y')$	RR	$xy(yx)$	$x'y'(y'x')$	RL
$A_{1g} + B_{1g}$	$A_{1g} + B_{2g}$	$A_{1g} + A_{2g}$	$A_{2g} + B_{2g}$	$A_{2g} + B_{1g}$	$B_{1g} + B_{2g}$

In the experiment contributions from sums of symmetries are measured, for instance

[2] The A_{2g} symmetry is not projected out, as the chiral excitation necessary is not present in the electron bands [31]

xx (read: polarisation vectors incoming-outgoing $\Rightarrow$ $x - x$) which gives contributions from both, A_{1g} and B_{1g} symmetries. Tab. 3.2 shows an overview. One can extract the sole contributions by measuring corresponding symmetries and solve the system of linear equations. For instance the B_{1g} contribution can be extracted by performing measurements in xx, $x'x'$ and RL:

$$R(B_{1g}) = \frac{1}{2}(xx - x'x' + RL) \tag{3.20}$$

R means the transition rate. This is not always necessary, as the A_{2g} contributions have been shown to be negligible in some cases due to a lack of accessible excitations [31]. In this case measurements containing A_{2g} already deliver the sole contribution from the corresponding symmetry.
Fig. 3.4 illustrates the selection rules in terms of the incoming (red) and outgoing (blue) polarisation vectors.

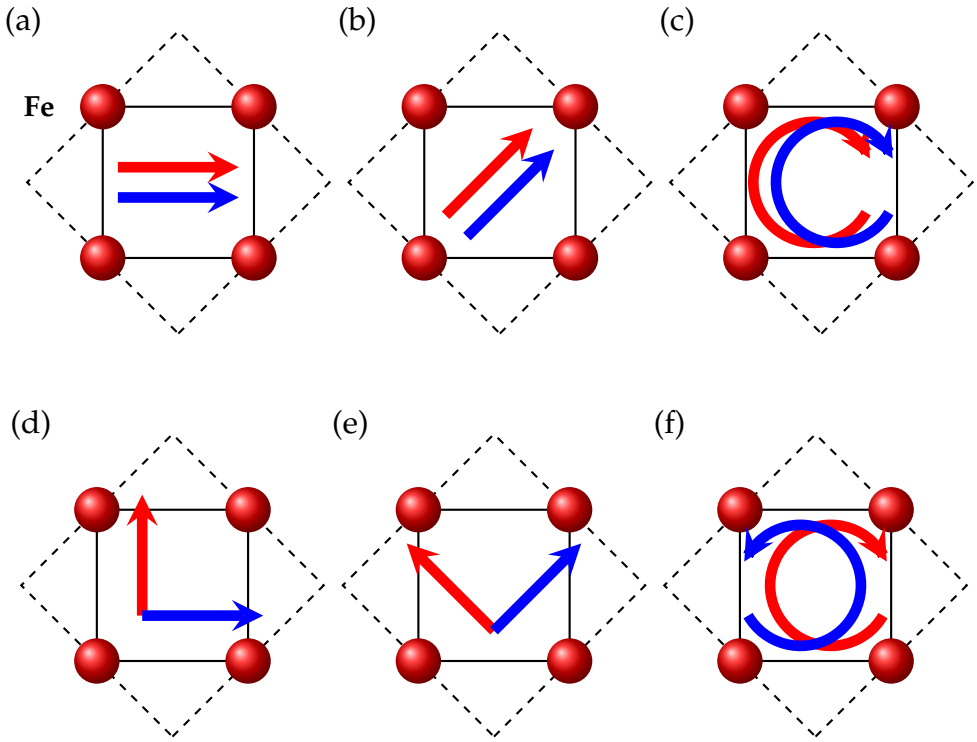

Figure 3.4.: Selection rules in $BaFe_2As_2$ [28]. The 1 Fe unit cell is displayed with a solid line, the 2 Fe unit cell with a dashed line. Blue arrows indicate the polarisation of the incident light and red arrows the polarisation of the scattering light. Polarisations according to Tab. 3.2.
3.4a: $xx(yy)$ 3.4b: $x'x'(y'y')$ 3.4c: RR
3.4d: $xy(yx)$ 3.4e: $x'y'(y'x')$ 3.4f: RL.

4. Experimental setup

Experiments were conducted in the Raman Lab I. The development and configurations of the setup are described in the references [33, 34, 28, 35, 36, 12] which Sec. 4.1 refers to. It is followed by a short description of the T_c measurement in Sec. 4.2.

4.1. Raman spectroscopy

A schematic representation of the Raman setup is depicted in Fig. 4.1. As light source serves either an Ar^+-laser (Coherent Innova 304C) with laser lines 514 nm $\geq \lambda_{exc} \geq$ 458 nm or a solid state laser (Coherent Genesis MX SLM 577-500) with a single line at $\lambda_{exc} = 575$ nm.
The beam is directed through a spatial filter consisting of an achromat followed by a circular aperture and another achromat (SP1). The achromats share the same focal point. The first achromat focuses the non-divergent parts of the beam in the centre of the aperture and divergent parts are blocked as they do not meet in the focal point. The second achromat parallelises the beam. This filters plasma lines of the laser resulting from other transitions within the laser medium.
The prism monochromator (PMC) refracts the beam and light with wavelengths deviating from the desired excitation wavelength are blocked by a slit with a resolution of 30 cm^{-1}.

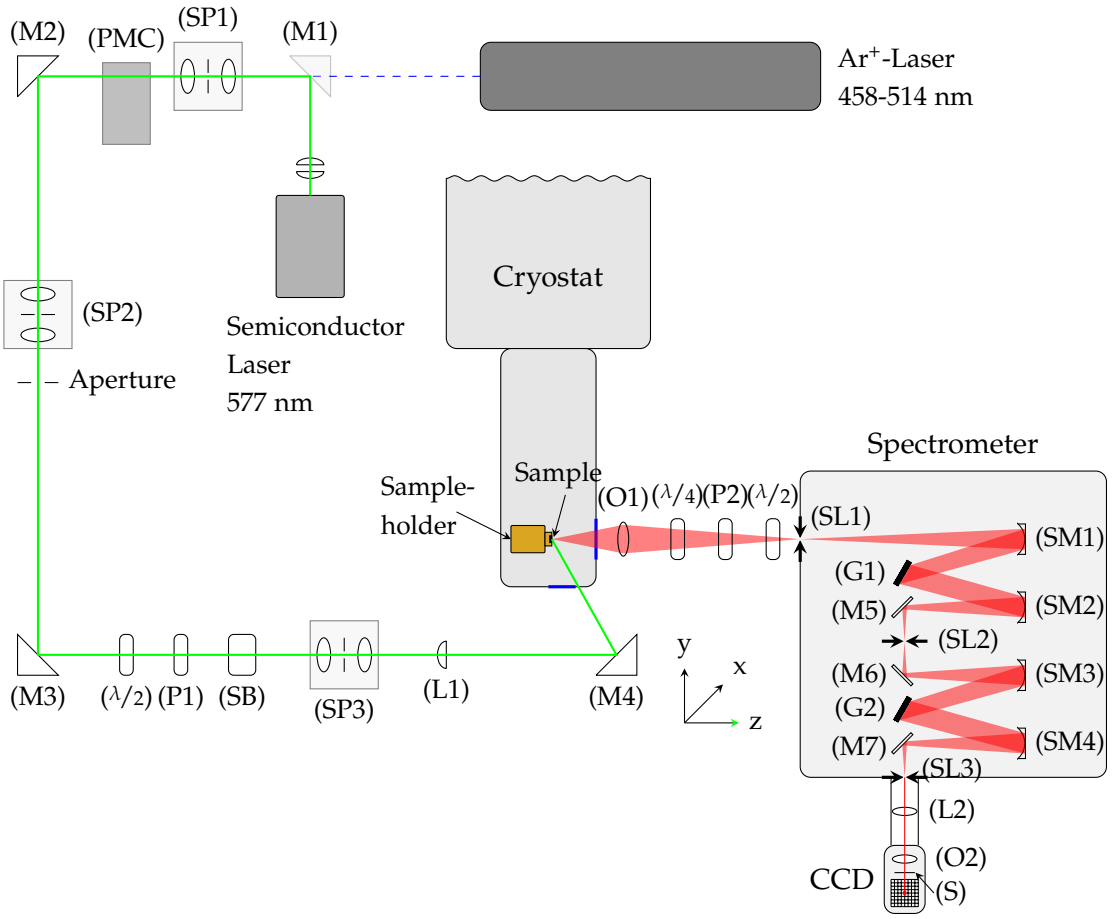

Figure 4.1.: Scheme of the Raman experiment in Raman Lab I. For details see text. Adapted from [28].

The laser power is adjusted by a first $\lambda/2$-retarder. The polarisation configuration is selected with a polariser and a Soleil-Babinet compensator (SB). A Soleil-Babinet compensator is a zero-order retarder and consists of an adjustable birefringent wedge and one, that is fixed to a polariser plate. In zero position the optical path in the medium of the wedges is as long as it is in the compensator plate. A phase difference is achieved by adjusting the movable wedge as this delays the parts of the linearly polarised beam which are perpendicular to each other. Such a phase difference results in elliptically polarised light.
The last spatial filter (SP3) ensures a Gaußian beam profile, and the beam is focused onto the sample by a lens (L1) and a mirror (M4). The sample is attached to a sample holder which is thermally coupled to the cryostat within the vacuum chamber.

Achievable temperatures range from 1.8 K to 340 K and the vacuum is of the order $p < 10^{-6}$ mbar.
As Raman scattering takes place only light emitted into a solid angle of approximately 0.2° around the sample's surface normal reaches the spectrometer. The optical axis of the spectrometer is parallel to the z axis of the lab system. The lens (O1) harvests the scattering light. Similar to the optical system which sets the incident polarisation a configuration consisting of a $\lambda/4$-retarder and a polariser is needed selects the outgoing polarisation. As for linearly polarised light, the $\lambda/4$ retarder is adjusted to the transmission axis of the polariser (P2). By rotating the $\lambda/4$-retarder by $\pi/4$ relative to the analyser one can select circular polarisations. The $\lambda/2$-retarder then rotates the pre-selected scattering light into the x-axis, i. e. the axis of maximum transmission of the spectrometer. The scattering light then enters the spectrometer through the first slit (SL1).
The spectrometer (Jarell-Ash 25-100 double monochromator) accommodates four spherical mirrors (SM) and two gratings (2400 lines/mm) as shown in 4.1. The entrance slit is in the focal plane of the first mirror which makes the divergent incoming light parallel before it arrives at the first grating. The light diffracted at the grating reaches the second mirror under wavelength-dependent angles and is refocused on the intermediate slit (SL2). The width of SL2 determines the spectral band selected. The light transmitted through SL2 experiences a path reversed to that of the first stage (subtractive dispersion). Consequently, the light at the exit slit (SL3) is white within the band selected by SL2. The exiting photons are detected by a charge-coupled device (CCD) operated at −110° C. Its efficiency is close to 90%.

4.2. T_c measurement setup

The setup used for the determination of the transition temperature T_c was constructed by Francesca Venturini (for technical details see [37]) and measures the third harmonic of the magnetic susceptibility $\chi_m(3f)$. This is done by applying a harmonic electromagnetic signal with a frequency f which induces an ac current in the sample. The temperature dependence of $\chi_m(3f)$ was derived by Yeshurun [38] on the basis of the Bean model [39]. The anharmonic contributions are small above T_c. Well below T_c the critical supercurrent I_c is much stronger than the current $I(H_f)$ induced by the field. But at T_c the density of the supercurrent is zero. The magnetc field can penetrate the sample. and the response to the time dependent electromagnetic field contains anharmonic components.

5. Spin-driven nematicity in $Ba(Fe_{0.949}Co_{0.051})_2As_2$

This chapter presents a study of fluctuations in $Ba(Fe_{0.949}Co_{0.051})_2As_2$ as observed by Raman scattering. The increase of spectral weight in the B_{1g} symmetry when approaching T_s will be identified as contribution from spin fluctuations. This contribution increases towards the structural transition and disappears upon magnetic ordering at T_{SDW}.
Following the analysis described in [12] this work could extend the spin fluctuation picture beyond the doping level of 2.5 %, which marks the onset of superconductivity. For this, the transition temperature of the structural and the magnetic transition T_s and T_{SDW}, respectively, were pinned down experimentally. After that, the onset temperature T_f of the fluctuations was determined. This was done by comparing relaxation rates in A_{1g} and B_{1g} symmetry with in plane resistivity measurements. The pile up of spectral weight in the B_{1g} symmetry was accounted for by an analysis of the Aslamazov-Larkin fluctuations. In this picture spin fluctuations are the most likely candidate to be driving the series of phase transitions in $Ba(Fe_{0.949}Co_{0.051})_2As_2$.

5.1. Determination of T_s and T_{SDW}

The determination of the temperatures T_s and T_{SDW} is crucial for the interpretation of the Raman spectra.
As for the structural transition, the orthorhombic distortion of the tetragonal lattice yields twin boundaries as described in Sec. 2.1. These twin boundaries reveal themselves as stripes on the sample's surface (Fig. 5.1 (a)). This is due to the accumulation of surface layers at these twin boundaries. To determine T_s one utilizes that the sample absorbs a known fraction of the incoming laser power P_{abs}, which heats it in proximity of the laser spot T_{spot} above the temperature of the sample holder T_h. This can be used to pin down T_s and also the effective laser heating $\Delta T = T_{spot} - T_h$ of the sample. Fig. 5.1 (a) shows the first occurrence of the stripes at $T_{Stripes} = 56.4$ K for $P_{abs} = 3$ mW. Observing the occurrence of the stripes for various absorbed laser powers as depicted in Fig. 5.1 (b) and Exploiting the linear trend, an extrapolation to zero power yields a

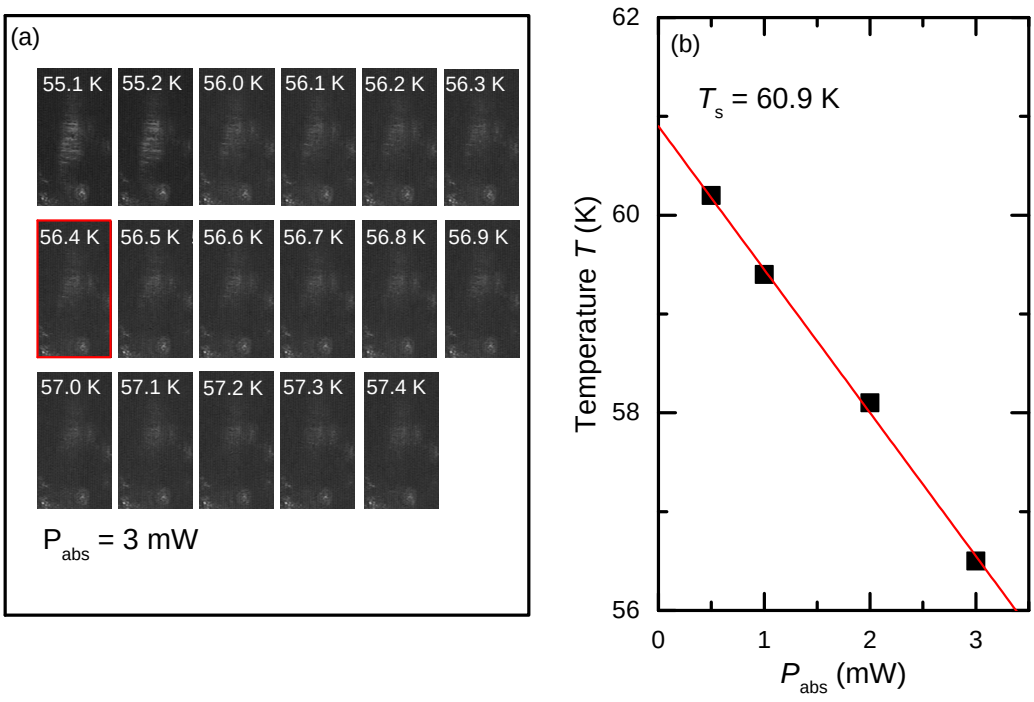

Figure 5.1.: Stripes appearing upon cooling through T_s in $Ba(Fe_{0.949}Co_{0.051})_2As_2$ due to the formation of twin boundaries, exemplary for the absorbed laser power $P_{abs} = 3$mW depicted in (a). The black squares in (b) represent the holder temperature $T_h(P_{abs})$ at which the stripes disappear. The red line extrapolates to the transition temperature for no heating to be $T_s = (60.9 \pm 0.1)$ K.

transition temperature $T_s = 60.9$ K. The laser heating is $\Delta T = 1.45$ K/mW.
For the determination of T_{SDW} the appearance of the A_{1g} phonon in B_{1g} symmetry was exploited (see Fig. 2.3). The appearance of a Fano shaped phonon at 180 cm $^{-1}$ in the B_{1g} symmetry coincides with the magneto-structural transition in the undoped compound $BaFe_2As_2$. Here, the magnetic and structural transition are not separated and it cannot be determined which of the two transitions is responsible for the symmetry breaking. Upon electron doping, the transitions are separated by ΔT (see Fig. 2.4) and the phonon is observed at the magnetic transition for a doping concentration $x = 0.025$ [12]. This behaviour was exploited for the $Ba(Fe_{0.949}Co_{0.051})_2As_2$ as well. The determination of T_{SDW} was done by measuring Raman spectra in small steps below T_s until the Fano shaped phonon appeared, as depicted in Fig. 5.2 (a). The phonon intensity was deter-

mined under the assumption that the particle-hole continuum is linear in an energy region close to the phonon line at 180 cm $^{-1}$. This linear continuum $R\chi''_{\text{linear p−h cont.}}$ was subtracted from the data $\Delta R\chi'' = R\chi''_{\text{spectrum}} - R\chi''_{\text{linear p−h cont.}}$. The intensity was calculated in terms of the area of the phonon's resonant part $|A_{\text{resonance}}|$ and its antiresonant part $|A_{\text{antiresonance}}|$ as $|A| = |A_{\text{resonance}}| + |A_{\text{antiresonance}}|$. Taking the antiresonance into account as well is justifiable, because the line shape of the phonon is affected by the magnetic ordering below T_{SDW}.
The intensity of the phonon is plotted against temperature in Fig. 5.2 (b) and shows an increase of intensity towards 50.0 K with a relatively constant intensity for $T < T_{SDW}$. The temperature of the magnetic transition was determined to be $T_{SDW} = 50.0$ K. In the region $T_s > T > T_{SDW}$ the intensity is approximately linear dropping to zero close to 59.3 K.

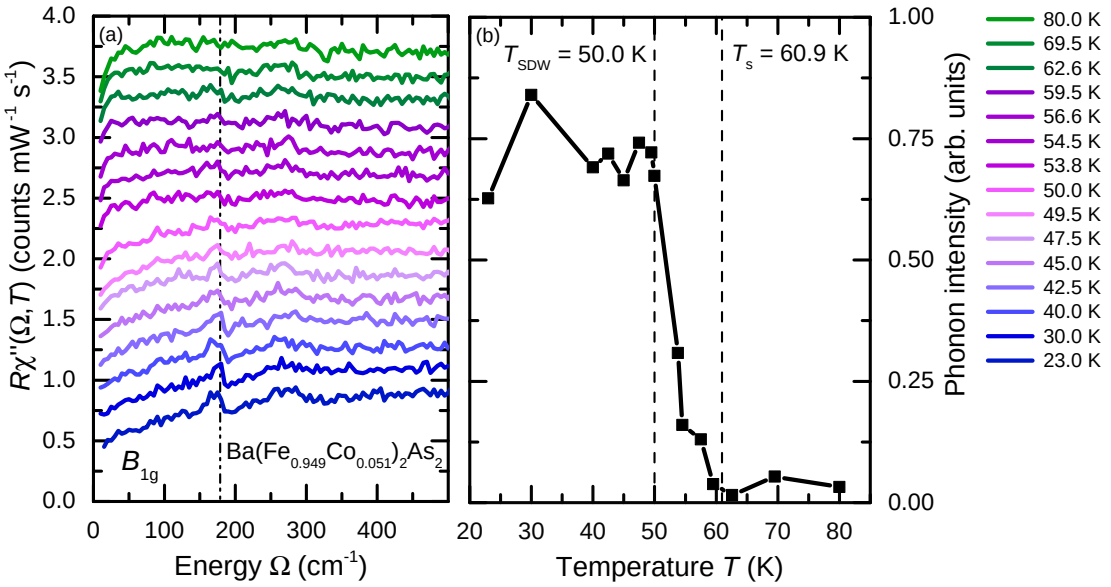

Figure 5.2.: B_{1g} spectra and phonon intensities. (a) Below the structural transition at T_s a symmetry-forbidden phonon appears in the position of the A_{1g} As mode. Below T_{SDW} an anti-resonance typical for a Fano interference can be observed. (b) Integrated intensity of the forbidden line as a function of temperature.

A qualitative comparison of the behaviour of intensity and the fluctuations, which will be discussed in Sec. 5.4, indicates a connection between fluctuations and the

appearance of the A_{1g} phonon line below T_s. But whether the phonon appears already at T_s and gains its Fano shape upon magnetic ordering or whether it appears only at T_{SDW} is yet to be determined. The phonon data obtained in the course of this thesis were not entirely conclusive. For further insight detailed measurements at other doping levels are necessary. Albeit pointing out the uncertainty at which temperature the phonon appears first, the Fano shape is very likely to develop upon magnetic ordering. This was indicated by results of samples of other doping concentrations thus far [12] and is a good parameter to pin down T_{SDW}.

5.2. Experimental results $Ba(Fe_{0.949}Co_{0.051})_2As_2$

Raman spectra of the $Ba(Fe_{0.949}Co_{0.051})_2As_2$ are shown in Fig. 5.3. The A_{1g} spectra in (a) are adopted from [32]. Three phonons are present for all temperatures, identified as the A_{1g} phonon at 180 cm $^{-1}$ and the two E_g phonons at 120 cm $^{-1}$ and 265 cm $^{-1}$ (see Fig. 2.3). The particle-hole (p-h) continuum is approximated with Eqn. 5.7 and depicted exemplarily for two temperatures along with their corresponding spectra in Fig. 5.3 (d).

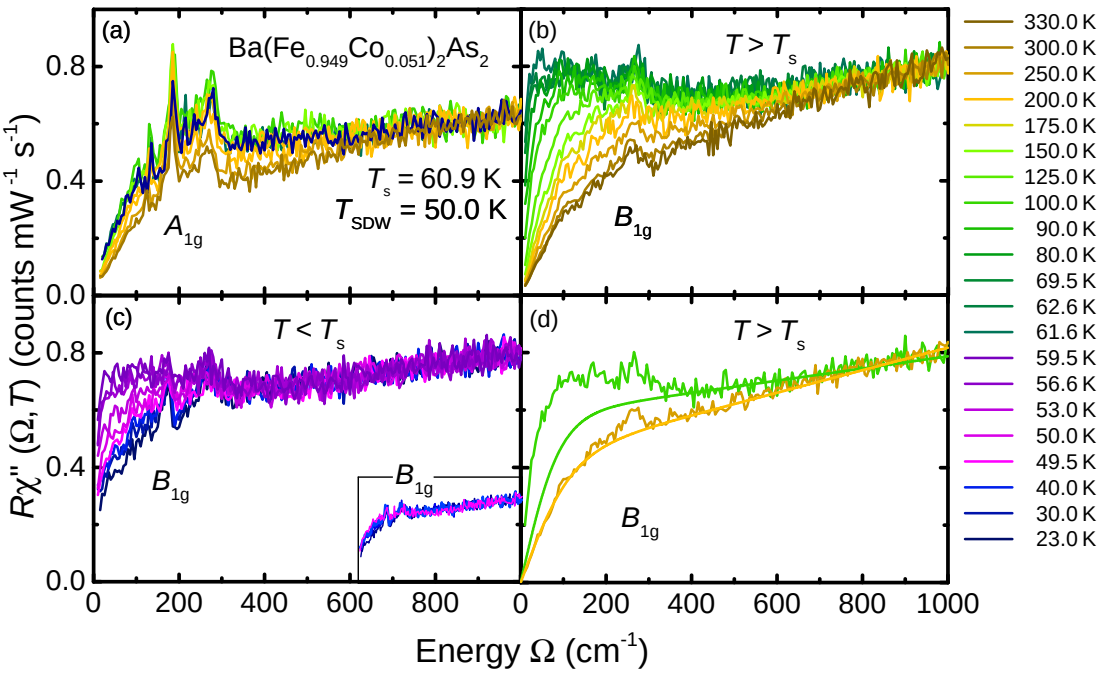

Figure 5.3.: Raman response of $Ba(Fe_{0.949}Co_{0.051})_2As_2$. (a) Spectra in A_{1g} symmetry for different temperatures above as well as below T_s and B_{1g} symmetry (b) above and (c) below T_s. The A_{1g} spectra are adopted from [32]. The inset in (c) shows B_{1g} spectra below T_{SDW}. Two p-h continuum fits are plotted exemplarily for 250 K and 90 K in (d) along with the corresponding spectra.

The A_{1g} spectra exhibit a small temperature dependence. The temperature trend of the B_{1g} spectra in Fig. 5.3 above and below T_s in (b) and (c), respectively, presents a different picture. An enhancement of the Raman response in B_{1g} symmetry is obvious for temperatures lower than $T < 300$ K. The low energy response is stronger than the response expected from approximation of the particle-hole continuum (see Eqn. 5.7) as shown in Fig. 5.3 (d) for 90 K. The additional spectral weight can be attributed to spin fluctuations, which will be discussed in Sec. 5.4.

5.3. Analysis

In order to extract the fluctuation contribution from the Raman response of the p-h continuum, further analysis is needed. The analysis rests on the assumption that the p-h continuum reflects the transport properties. In addition, the A_{1g} and B_{1g} symmetry

spectra exhibit similar dynamic behaviour and compare well to the static relaxation found by resistivity measurements. The first step is to pin down the temperature T_f at which the two Raman symmetries develop different temperature dependencies and deviations from transport measurements can be observed.

5.3.1. Relaxation rate analysis

Transport measurements extract resistivities which relate to a scattering time τ. This can also be derived from the Raman spectra. The static limit, as corresponding to large time scales, is obtained from the imaginary part of the Raman response χ'' at small energies. The relaxation rate in terms of the carrier lifetime $\tau_{\gamma\gamma}$ reads

$$\Gamma_{\gamma\gamma} = \frac{\hbar}{\tau_{\gamma\gamma}} \tag{5.1}$$

with the Raman vertex $\gamma = \gamma(\mathbf{k})$. These relaxation rates agree with transport measurements at high temperatures. Discrepancies between Raman and transport measurements would point directly to an additional contribution to the Raman response which is the case for the $Ba(Fe_{0.949}Co_{0.051})_2As_2$.
Opel *et al.* [40] showed that the memory function approach, originally suggested by Götze and Wölfle [41] for optical spectroscopy, can be applied to Raman spectra. The imaginary part of the Raman spectral function $\chi''_{\gamma\gamma}(\Omega, T)$ can be written in terms of the dynamic relaxation rate $\Gamma_{\gamma\gamma}(\Omega, T)$ and the mass enhancement factor $1 + \lambda_{\gamma\gamma}(\Omega, T)$ [42]:

$$\chi''_{\gamma\gamma}(\Omega, T) = \frac{\Omega\Gamma_{\gamma\gamma}(\Omega, T)}{\Omega^2[1 + \lambda_{\gamma\gamma}]^2 + \Gamma^2_{\gamma\gamma}(\Omega, T)}. \tag{5.2}$$

$\Gamma_{\gamma\gamma}(\Omega, T)$ and $1 + \lambda_{\gamma\gamma}(\Omega, T)$ are both symmetry resolved, i.e. project different parts of the Brillouin zone as they depend on the form factor $\gamma(\mathbf{k})$. Extracting $\Gamma_{\gamma\gamma}(\Omega, T)$ from the A_{1g} and B_{1g} spectra yields symmetry resolved relaxation rates.
Figure 5.4 shows the dynamic relaxation rates in A_{1g} symmetry for $T > T_s$ as well as $T < T_s$. Especially the comparison with the B_{1g} spectra in Fig. 5.5 (a) and (b) shows a qualitative difference in the temperature evolution of A_{1g} and B_{1g} relaxation rates. Similar to the Raman spectra in Fig. 5.3 the A_{1g} relaxation rates show a small temperature dependence. The B_{1g} relaxation rates depicted in Fig. 5.5 (a) and (b) for $T > T_s$ and $T < T_{SDW}$ exhibit a small temperature dependence comparable to the A_{1g} relaxation rates for $T > 175$ K. However , the temperature dependence deviates more for 175 K $> T > T_s$. The extraction of the static relaxation rates $\Gamma(\Omega \to 0, T) = \Gamma_0(T)$ makes this more evident for which additional analysis is needed.

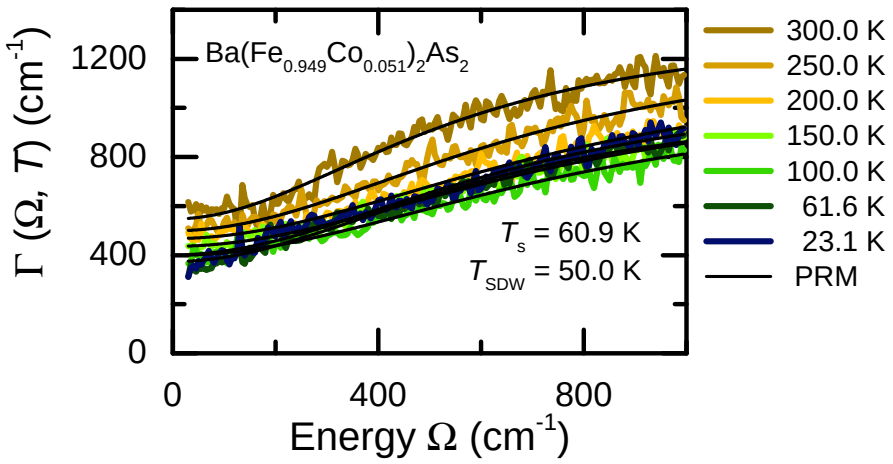

Figure 5.4.: Dynamic relaxation rates for the A_{1g} spectra for $T > T_s$ and $T < T_s$. The black lines indicate the resulting fits from the parallel resistor model (PRM) as described in detail below (Eqn. 5.4) .

As can be seen from Fig. 5.5 (a) for $T > T_s$ and in (b) for $T < T_s$, the dynamic relaxation rates derived from the Raman response $R\chi''_{\gamma\gamma}(\Omega, T)$ drop towards zero in the vicinity of $\Omega = 0$. This can be attributed to the fluctuation contribution to the Raman response. The fluctuations are additive to the p-h continua (see Subsec. 5.3.2) of the Raman spectra and yield higher intensities, which in turn lead to lower relaxation rates. To extract the static relaxation rates (i. e. the intercept with the y-axis), it is necessary to fit the data with an appropriate model - in this case the parallel resistor model (PRM). The corresponding fits in figures 5.4 and 5.5 are denoted as black lines. A detailed description of the model can be found in [43]. A short summary of the model is given in the following.

The total dynamic relaxation rate $\Gamma_{\gamma\gamma}(\Omega, T)$ is expressed in terms of a low frequency part $\Gamma^*_{\gamma\gamma}(\Omega, T)$ and a high frequency part $\Gamma^{\max}_{\gamma\gamma}(T)$. This *ansatz* uses Kirchhoff's law for resistors, in which the overall resistivity of resistors connected parallel is simply given by $1/\rho = \sum_i 1/\rho_i$. From Eqn. 5.1 it is easy to see, that $\rho \propto \Gamma_{\gamma\gamma}$ holds and the total dynamic relaxation rate is given by

$$\frac{1}{\Gamma_{\gamma\gamma}(\Omega, T)} = \frac{1}{\Gamma^*_{\gamma\gamma}(\Omega, T)} + \frac{1}{\Gamma^{\max}_{\gamma\gamma}(T)}. \tag{5.3}$$

The low frequency part is written as $\Gamma^*_{\gamma\gamma}(\Omega, T) = c(T) + a(T)\Omega^2$ with temperature dependent parameters $a(T)$ and $b(T)$ [43], which has been a good methodology in cuprates [40]. In the $\Omega \to \infty$ regime, the Mott-Ioffe-Regel (MIR) limit is applicable.

This limit states, that a lower boundary exists for the mean free path of the electrons within the crystallographic unit cell. The relaxation rates converge towards a maximum rate $\Gamma_{\gamma\gamma}^{\max}$.
The dynamic relaxation rate is obtained via inversion of Eq. 5.3

$$\Gamma_{\gamma\gamma}(\Omega, T) = \frac{\Gamma_{\gamma\gamma}^{\max}(T) \cdot (c(T) + a(T) \cdot \Omega^2)}{\Gamma_{\gamma\gamma}^{\max}(T) + c(T) + a(T) \cdot \Omega^2} \tag{5.4}$$

with which the empirical relaxation rates were fitted, as indicated by the black lines in Fig. 5.4 and Fig. 5.5 (a) and (b). The static limit is derived from the dynamic relaxation rates. This means:

$$\Gamma_0(T) = \Gamma_(\Omega \to 0, T) = \lim_{\Omega \to 0} \frac{\Gamma_{\gamma\gamma}^{\max}(T) \cdot (c(T) + a(T) \cdot \Omega^2)}{\Gamma_{\gamma\gamma}^{\max}(T) + c(T) + a(T) \cdot \Omega^2} = \frac{\Gamma_{\gamma\gamma}^{\max}(T) \cdot c(T)}{\Gamma_{\gamma\gamma}^{\max}(T) + c(T)} \tag{5.5}$$

The static limit of the relaxation rate also yields an expression for the temperature dependent dc-resistivity $\rho(T)$ of a metal[1] [40]

$$\Gamma_0(T) = \frac{1}{\tau_0(T)} = 1.08 \cdot \rho(T) \cdot \omega_{\mathrm{Pl}}^2 \tag{5.6}$$

with the material dependent plasma frequency ω_{Pl}.
The fit described by Eqn. 5.4 yields the dynamic relaxation rates depicted in Fig. 5.4 and Fig. 5.5 (a) and (b), and show good agreement with the experimental relaxation rates for high energies. The static relaxation rates obeying the limit of Eqn. 5.5 can be found in (c) and the region close to the magneto-structural phase transition in (d). If one had considered the intersect of the B_{1g} relaxation rate data rather than the static limit of Eqn. 5.4, one would have obtained the same qualitative trend.

[1] Iron pnictides are quite metallic. More than the cuprates as they are ceramics.

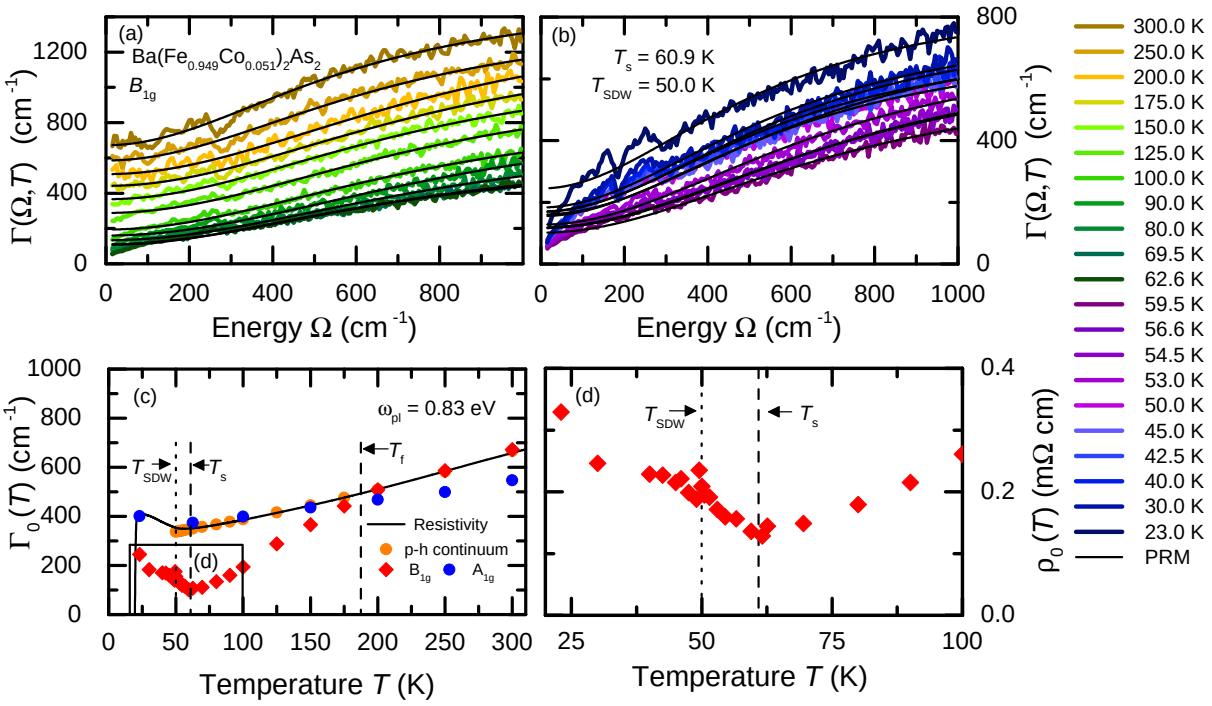

Figure 5.5.: Dynamic relaxation rates. (a) above T_s and (b) below T_s. The black lines indicate the resulting fits from the parallel resistor model (PRM). In (c) the direct comparison of the static relaxation rates from the A_{1g} and B_{1g} spectra is shown along with the one's from the p-h continua approximation (orange) and the resistivity (black).(d) The region around T_s and T_{SDW} is rescaled and converted to mΩ cm.

The relaxation rates of the p-h continua are drawn as orange circles in Fig. 5.5 (c). They are fit parameters in Eqn. 5.7 and were chosen to reproduce the resistivity (black curve). While the A_{1g} static relaxation rates follow the general trend of the transport measurement to 23.0 K the B_{1g} static relaxation rates start to differ in the range 170 K $< T_f <$ 180 K. The deviation of the B_{1g} rates increases towards T_s and develops a minimum at T_s. Towards T_{SDW} it increases with a discontinuity at the magnetic transition. The onset of the fluctuations was determined to be in a window around $T_f = 175$ K. With T_f being pinned down the fluctuation contribution can be extracted.

5.3.2. Aslamazov-Larkin fluctuations

As stated above the pile up of the B_{1g} spectra towards T_s cannot be explained by the temperature dependence of the p-h continuum. For the following analysis we assume that the p-h continuum and the superposed intensity are additive. Then the p-h continuum can be subtracted out.

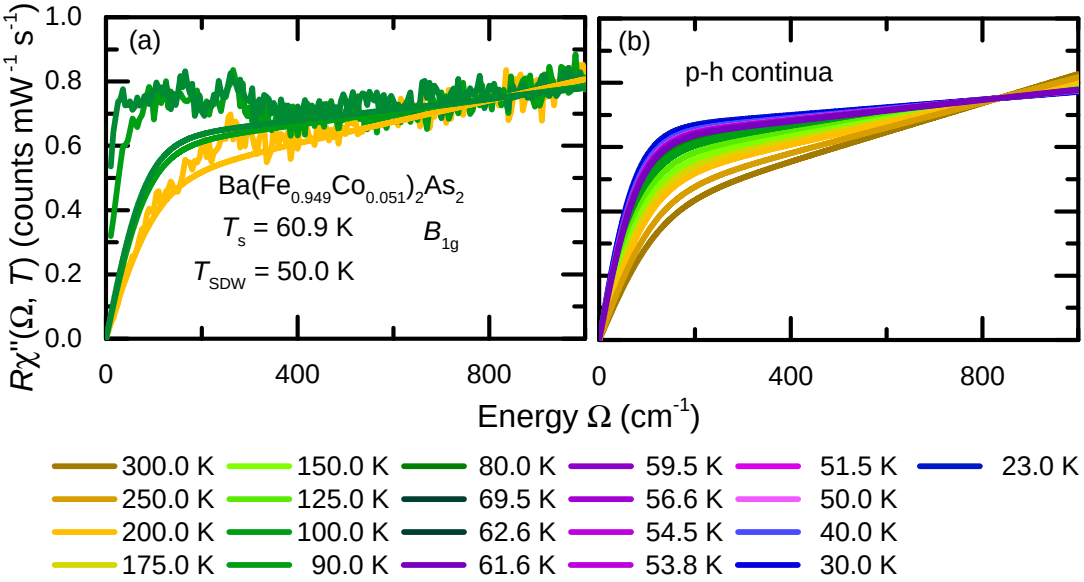

Figure 5.6.: Three Raman spectra in (a) in B_{1g} symmetry with the corresponding p-h fits above T_s. The yellow curves correspond to $T = 200.0$ K and are above T_f. In (b) the temperature dependent p-h continua fits are depicted.

Illustrated in Fig. 5.6 (a) are three Raman spectra in comparison with the p-h continuum fits for the corresponding temperatures. The fits obey [18]

$$\chi''_{\text{cont}}(\Omega, T) = \underbrace{[\alpha_1 + \alpha_2 \cdot T]}_{\text{low energy behaviour}} \cdot \tanh\left(\frac{\Omega}{\tilde{\Gamma}_0(T)}\right) + \underbrace{[\beta_1 + \beta_2 \cdot T]}_{\text{high energy behaviour}} \cdot \frac{\Omega}{\tilde{\Gamma}_0(T)} \tag{5.7}$$

with $\alpha_1 = 0.3752$, $\alpha_2 = -0.0010$ and $\beta_1 = 0.000452001$, $\beta_2 = 0.0000012$. The first bracket attributes the linear behaviour in the low energy part of the spectra and the second bracket the linear behaviour for higher energies. The fit parameter $\tilde{\Gamma}_0(T)$ is chosen so that the inverse slope $\Gamma_0(T)$ of $\chi''_{\text{cont}}(\Omega, T)$ reproduces the in-plane resistivity (see orange circles in Fig. 5.6). The quality of the model can be checked for $T > T_f$ where satisfactory agreement between the static relaxation rates derived from the model, the

data and the resistivity is achieved. Thus, it seems reasonable to substract the p-h continua from the Raman spectra to extract the fluctuation contribution.

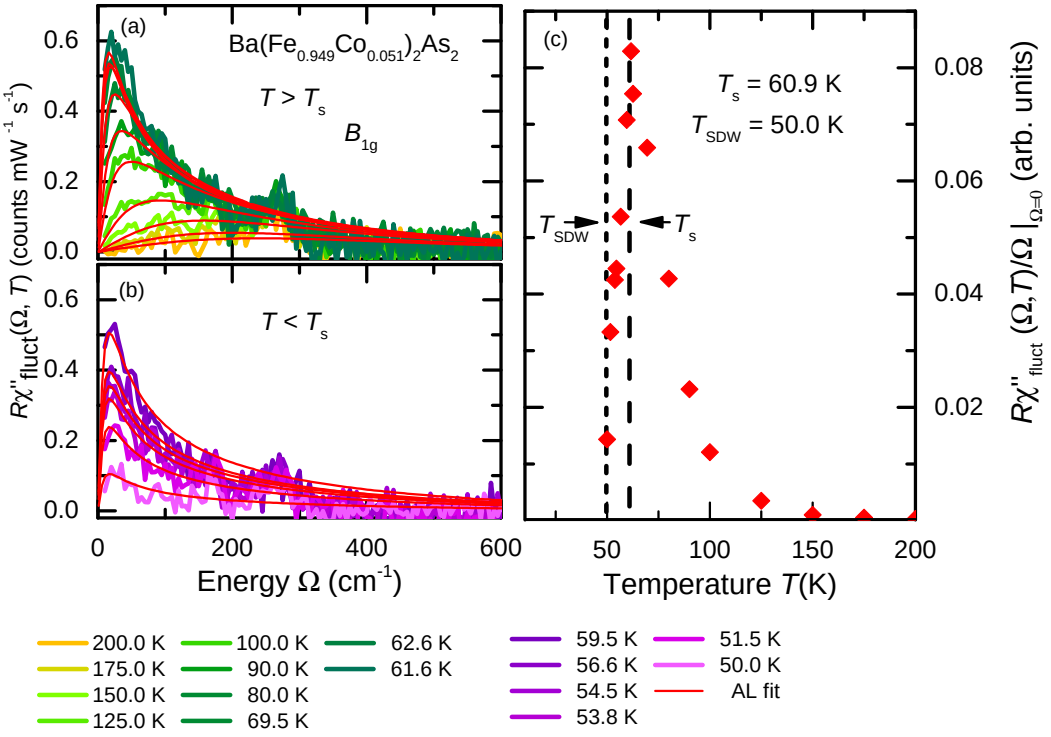

Figure 5.7.: Bare fluctuation contribution of the spectra for (a) $T_f > T > T_s$ and (b) $T_s > T > T_{SDW}$. The red lines describe the AL fit. The initial slopes of those fits were extracted and plotted against the temperature in (c) (red squares).

This subtraction yields the bare fluctuation contribution to the spectra as depicted in Fig. 5.7 (a) above the structural phase transition and (b) below T_s. For $T > T_s$ an increase of the fluctuation contribution is observed as one goes towards T_s with the emergence of a hump at 175.0 K to a defined peak above T_s. As the Raman response converges towards the p-h continua given by Eqn. 5.7 for higher energies, the fluctuation response converges to zero.

Caprara *et al.* [42] showed that a contribution $\Delta\chi''_{\gamma\gamma}$ resulting from spin and/or charge fluctuations can be described by

$$\Delta\chi''_{\gamma\gamma} = \Lambda^2_{\gamma\gamma} \int_0^\infty \mathrm{d}z \left[b\left(z - \frac{\Omega}{2}\right) - b\left(z + \frac{\Omega}{2}\right) \right] \frac{z_+ z_-}{z_+^2 - z_-^2} \left[F(z_-) - F(z_+) \right] \tag{5.8}$$

in which $b(z)$ represents the Bose distribution function, $\Lambda^2_{\gamma\gamma}$ the symmetry coefficient

(see Eqn. 5.11) and

$$F(z) = \frac{1}{z}\left[\arctan\left(\frac{\Omega_0}{z}\right) - \arctan\left(\frac{m(T)}{z}\right)\right] \tag{5.9}$$

with $z_\pm = [z \pm \Omega/2][1 + (z \pm \Omega/2)^2/\Omega_0^2]$, the mass $m(T)$ and $\Omega_0 \sim (100 - 500)$ cm^{-1}, an ultraviolet cutoff. The mass is inversely proportional to the square of the length scale ξ over which fluctuating order is established: $m(T) \propto 1/\xi^2$. The mass is plotted against the temperature for $T_{SDW} < T < T_f$ in Fig. 5.8. It decreases as one approaches T_s and stays constant in the nematic phase.

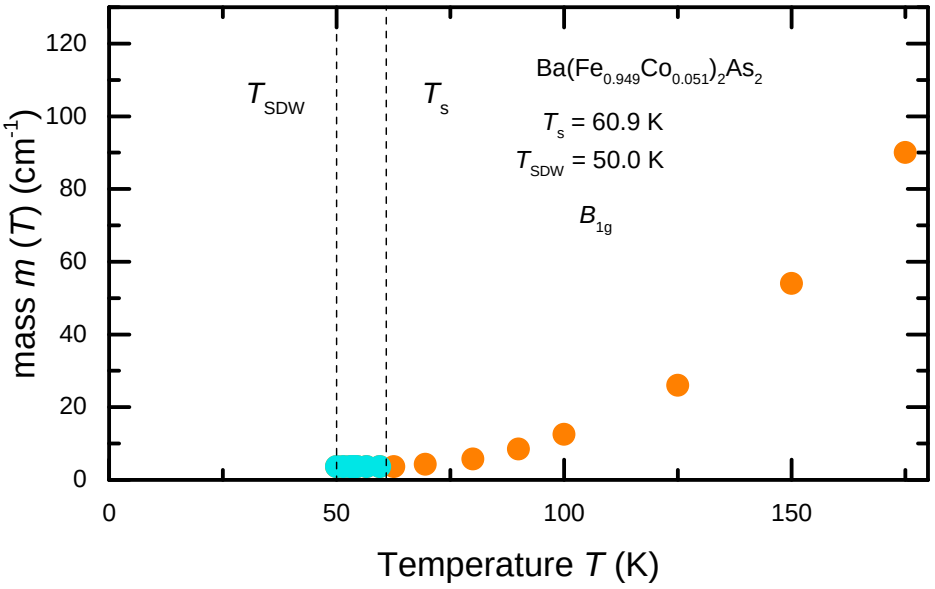

Figure 5.8.: Temperature dependence of $m(T)$. Upon lowering the temperature towards T_s the mass decreases and is constant in the nematic phase, i. e. $T_{SDW} < T < T_s$.

The approach is based on the work of Aslamazov and Larkin who described conductivity fluctuations, i. e. an increase of the conductivity, in superconductors setting in above T_c [44]. Therefore, the fluctuations are referred to as Aslamazov-Larkin (AL) fluctuations (see Feynman diagram in Fig. 5.9).
The red lines in Fig. 5.7 represent the approximation of the data on the basis of Eqn. 5.8. The agreement between fit and data as depicted in Fig. 5.7 (a) and (b) supports the interpretation in terms of thermal fluctuations. The model presented in the next

section shows, that the initial slopes of the AL fits are the proper parameter to describe the fluctuations. These initial slopes are given by

$$\frac{R\partial\chi''_{\text{fluct}}(\Omega,T)}{\partial\Omega}\,|_{\Omega\to 0}=\frac{R\chi''_{\text{fluct}}(\Omega,T)}{\Omega}. \tag{5.10}$$

The initial slopes are presented in Fig. 5.7 (c) and increase towards and develop a maximum at T_s. They do not disappear entirely in the nematic phase. Instead, they decrease continuously towards T_{SDW}. The disappearance of the fluctuations at the magnetic transition T_{SDW} supports a scenario, in which spin fluctuations contribute largely to the additional spectral weight in the temperature regime $T_{SDW} < T < T_f$.

5.4. Discussion - AL selection rules and spin fluctuations

The extra contribution to the low-energy Raman response shall be discussed in this section. A closer look is offered at the origin of this deviation and its behaviour close to the magneto-structural transition.

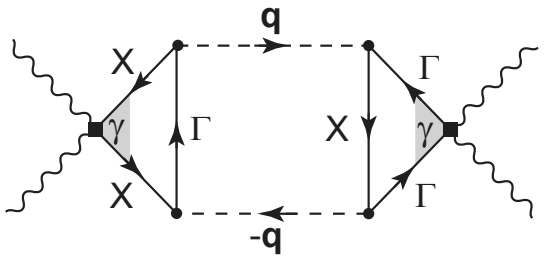

Figure 5.9.: Feynman diagram of the AL fluctuation contribution to the Raman response. The straight lines represent the usual electron propagators, the dashed lines the bosonic propagators and the squares mean the Raman vertex $\gamma(\mathbf{k})$. Adapted from [12].

Up to now, it has been established, that spin and/or charge [45] fluctuations can be hold accountable for the anomalous additional spectral weight in the low energy Raman spectra below T_f and above T_s. Here, the low energy Raman spectra are well described by Eqn. 5.8. Yet it is not clear which scenario is most appropriate, i. e. if the fluctuation contribution originates from spin or charge fluctuations or a mixture of both. Neither is clear, why the fluctuations appear only in the B_{1g} symmetry. The evaluation of the AL selection rules gives insight to these questions.

For this, the exchange of two fluctuations $\mathbf{q}$ and $-\mathbf{q}$ is considered. They sum up to zero and can be represented by the lowest order Feynman diagram in Fig. 5.9. The straight lines are the electron propagators $G_{\mathrm{i}}(\mathbf{k}, \omega)$ (in accordance with the notation used in [27]) and the bosonic propagator (dashed) reads

$$D(\mathbf{q}, \omega_{\mathrm{m}}) = \frac{1}{|\omega_{\mathrm{m}}| + \nu|\mathbf{q} - \mathbf{q}_{\mathrm{c}}| + m(T)} \tag{5.11}$$

with the Matsubara frequencies ω_{m}, a constant electronic energy scale ν and the mass $m(T)$. The wavevector $\mathbf{q}_{\mathrm{c}}$ of critical fluctuations is different for spin or charge fluctuations. For SDW ordering the vector is $\mathbf{q}_{\mathrm{c}} = (\pi, 0), (0, \pi)$. One may as well set $\mathbf{q}_{\mathrm{c}} = (\pi, 0)$ as all representations have the same pyhsical meaning here.
The fermionic loop (symmetry factor) resulting from the Green's functions and the Raman vertices $\gamma(\mathbf{k})$ reads

$$\Lambda_{\gamma\gamma}(\mathbf{q}, \Omega_{\mathrm{l}}, \omega_{\mathrm{m}}) = CT \sum_{\mathrm{n}} \sum_{\mathbf{k}} \gamma(\mathbf{k}) G(\mathbf{k}, \epsilon_n + \Omega_{\mathrm{l}}) G(\mathbf{k} - \mathbf{q}, \epsilon_{\mathrm{n}} - \omega_{\mathrm{m}} G(\mathbf{k}, \epsilon_{\mathrm{n}}). \tag{5.12}$$

Setting $\mathbf{q} = \mathbf{q}_{\mathrm{c}}$ gives the dominant contributions of the Feynman diagram as it maximises the propagator in Eqn. 5.11 for constant ω_{m}.
The sum over $\mathbf{k}$ vectors includes a sum over all Raman vertices $\gamma(\mathbf{k})$. This demands $\gamma(\mathbf{k})$ to not change signs between $\mathbf{k}$ and $\mathbf{k} + \mathbf{q}_{\mathrm{c}}$. In other words, contributions from Fermi sheets connected by $\mathbf{q}_{\mathrm{c}}$ can be expected if the sign of $\gamma(\mathbf{k})$ does not change.

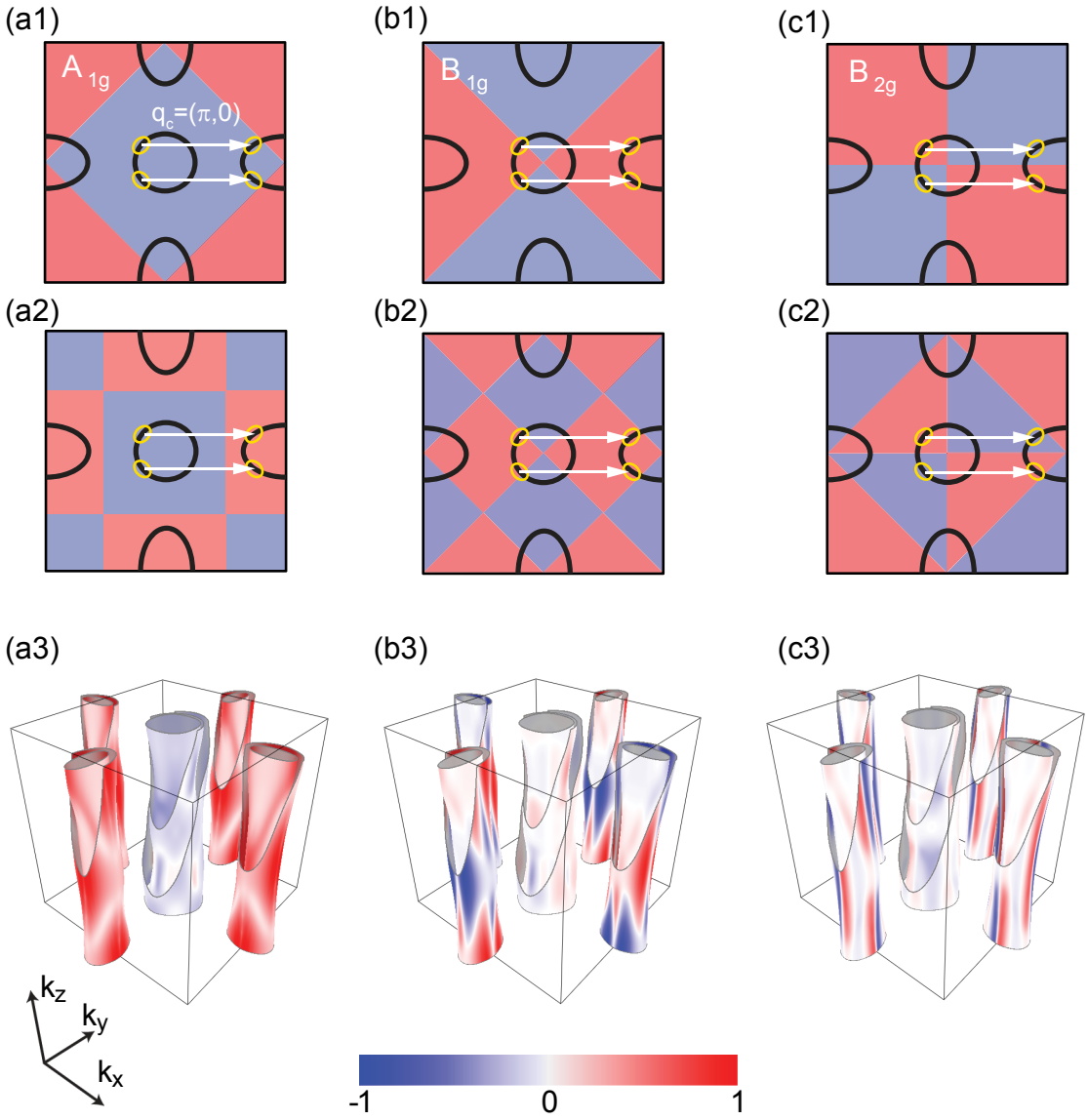

Figure 5.10.: AL selection rules in the BZ of the 1 Fe unit cell in iron arsenides. (a1)-(c1) and (a2)-(c2) show the vertices derived from the first and second order BZ harmonics in A_{1g}, B_{1g} and B_{2g} symmetries with the sign of the Raman vertex being positive (red) or negative (blue). The white arrow indicates the critical vector $\mathbf{q}_c$ which connects hole and electron pockets. (a3) to (c3) depict the vertices derived from the effective-mass approximation. From [46]. Adapted from [12].

The AL selection rules are depicted in Fig. 5.10 with the ordering or nesting vector $\mathbf{q}_c = (\pi, 0)$ projected onto the BZ of the 1 Fe unit cell. The yellow ellipses are so called hot spots at which the nesting conditions are locally improved. Perfect nesting is achieved, when this vector maps one FS exactly onto another. (a1) and (a2), (b1) and (b2) and (c1) and (c2) show the vertices derived from the first and second order A_{1g}, B_{1g} and B_{2g} BZ crystal harmonics. (a3) to (c3) show the vertices derived by the effecitve mass approximation in a tight binding model [46].
In terms of Fig. 5.10 contributions from fluctuations arise, if $\mathbf{q}_c$ connects Fermi sheets with the same colour (i. e. with the same sign for γ). This is not the case for the second order A_{1g} BZ harmonics (cf. (a2)) and both, first and second order, B_{2g} BZ harmonics (cf. (c1) and (c2)). Contributions should be expected from the first order A_{1g} BZ harmonics and the first and second order B_{1g} BZ harmonics. However, neither the A_{1g} Raman spectra nor the relaxation rates indicate an additional contribution due to fluctuations. Taking into account the vertices derived from the effective mass approximation in (a3) to (c3) explains the lack of a fluctuation contribution in the A_{1g} symmetry:
The BZ of the 1 Fe unit cell is drawn along $\mathbf{k}_x$, $\mathbf{k}_y$ and $\mathbf{k}_z$ as black box [46]. Three hole bands are visible at the centre and two electron bands at each face. The colours blue to red quantify the intensity and the sign of the Raman vertex as indicated by the colour scheme at the bottom of the figure. In (a3) the vertex in A_{1g} is negative for the hole pockets and positive for the electron pockets. In terms of BZ harmonics, the A_{1g} vertex has second order character in which the vertex changes its sign from one end of $\mathbf{q}_c$ to the other. This leads to cancellation of the fluctuation contribution.
In (b3) the vertex changes its character from first to second order and back to first order B_{1g} BZ harmonics. Neither order leads to cancellation effects and fluctuation contributions can be expected under consideration of both, AL selection rules and effective mass approximation.
The B_{2g} vertex is of second order and here all BZ harmonics lead to cancellation effects. Fluctuation contributions can not be expected.
The occurrence of the fluctuations solely in the B_{1g} symmetry is consistent with the AL selection rules with the critical vector $\mathbf{q}_c = (\pi, 0)$ and the effective mass approximation. This is a strong indication that spin fluctuations can be hold accountable for the pile-up in the B_{1g} spectra.
As illustrated in Fig. 5.7 (c) upon lowering temperature the initial slope diverges towards T_s and decreases towards T_{SDW} at which it finally disappears upon magnetic ordering. Spin fluctuations along $\mathbf{q}_c$ support an increase towards T_{SDW} followed by a sharp drop to zero as magnetic ordering is established (cf. Sec. 2.3).

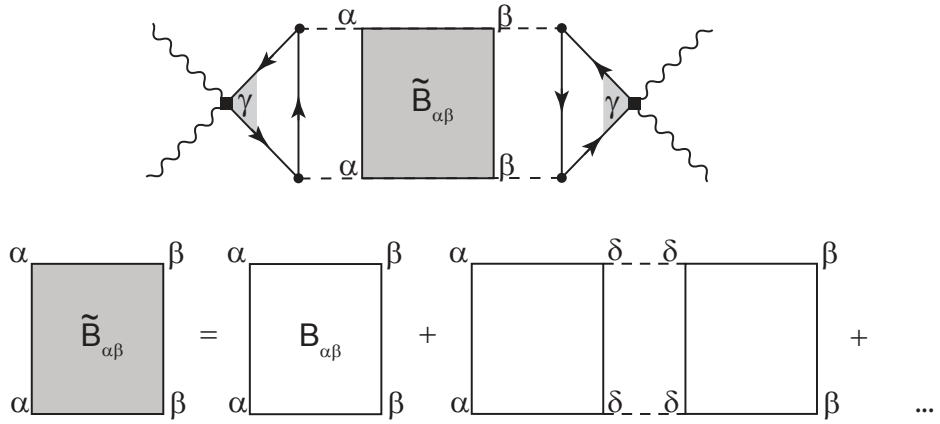

Figure 5.11.: Higher order AL diagrams considering interacting fluctuations. $\tilde{B}_{\alpha\beta}$ is the sum over boxes $B_{\alpha\beta}$ with the index $\alpha = X, Y$ the entering spin fluctuations and β the type of exiting spin fluctuations. Adapted from [12].

On the basis of the AL Feynman diagram in Fig. 5.9, one can explain the increase of the initial slopes towards T_s and the survival of the fluctuations in the nematic phase. For this, interactions between more than two fluctuations are considered as depicted in Fig. 5.11. The grey box stands for higher order fluctuation interactions.
This summation has a consequence for the Raman response function. Karahasanovic *et al.* [47] proposed an expression for the Raman response function in the case of interacting fluctuations for small frequencies Ω and an infinite sum over higher order AL diagrams (represented by the grey box). The resummed Raman response function is then given by

$$\tilde{R}(\Omega) = R_0(\Omega) \cdot (1 + g\chi^{\mathrm{el}}_{\mathrm{nem}}(0)) \tag{5.13}$$

with the noninteracting Raman response $R_0(\Omega)$. Eqn. 5.13 states the proportionality between the Raman response $\tilde{R}(\Omega)$ and the electronic nematic susceptibility $\chi^{\mathrm{el}}_{\mathrm{nem}}$ which is expressed in terms of the magnetic susceptibility $\chi_{\mathrm{mag}}(\mathbf{q})$:

$$\chi^{\mathrm{el}}_{\mathrm{nem}}(0) = \frac{\int_{\mathbf{q}} \chi^2_{\mathrm{mag}}(\mathbf{q})}{1 - g \int_{\mathbf{q}} \chi^2_{\mathrm{mag}}(\mathbf{q})}. \tag{5.14}$$

g is the nematic coupling constant. In Fig. 5.12 the BZ is depicted schematically along with the round hole pockets at the Γ point and the elliptic electron pockets at the X and Y points.

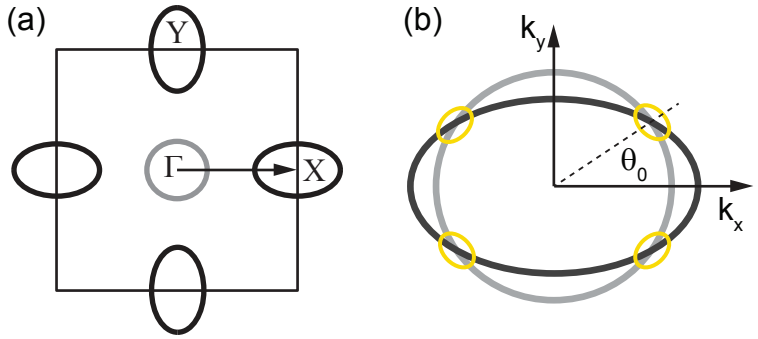

Figure 5.12.: Round hole bands around the Γ point in grey and slightly elliptic electron bands in black. The yellow ellipses denote hot spots at which the nesting conditions are locally improved. These are connected by the vector $\mathbf{q}_c$. From [12].

The yellow ellipses represent the hot spots occurring in Fig. 5.10. The nematic coupling constant is dependent on the ellipticity α of these electron pockets with $g = \alpha/T^4$. g has only a weak temperature dependence close to T_{SDW} and one can set $g(T) = g(T_{SDW})$.
So far, the groundwork was laid to explain the behaviour of the initial slopes in the tetragonal and nematic phase. In the following, it shall be shown how $\tilde{R}(\Omega)$ behaves for $T > T_s$ and in the nematic phase, i. e. in the regime $T_s > T > T_{SDW}$. It will be seen, that the following calculations reproduce qualitatively the behaviour depicted in Fig. 5.7 (c). Furthermore, the interpretation of the fluctuations in terms of the initial slopes of the AL fits given by Eqn. 5.10 will be justified.

Nematic susceptibility for $T > T_s$

As $\tilde{R}(\Omega) \propto \chi^{el}_{nem}$ an expression for χ^{el}_{nem} which is dependent on the magnetic susceptibility shall be derived for $T > T_s$.
Following the nomenclature in Sec. 2.3, $\chi_{mag}(\mathbf{q})$ means again the magnetic susceptibility. This magnetic susceptibility can be written as

$$\chi_{mag}(\mathbf{q}) = \frac{1}{T - T_{SDW} + (\mathbf{q} - \mathbf{q}_c)^2} = \frac{1}{r(T) + (\mathbf{q} - \mathbf{q}_c)^2} \tag{5.15}$$

which diverges along the critical vector, i. e. for $\mathbf{q} = \mathbf{q}_c$, at the magnetic transition temperature T_{SDW}. Integrating the expression in Eqn. 5.14 in two dimensions yields

$$\int_{\mathbf{q}} \chi^2_{mag}(\mathbf{q}) = \int_{\mathbf{q}} \frac{1}{(r(T) + (\mathbf{q} - \mathbf{q}_c)^2)^2} = \int_0^\infty dx \, \frac{1}{(r(T) + x)^2} = \frac{1}{r(T)} \tag{5.16}$$

with the substitution $x = (\mathbf{q} - \mathbf{q}_c)^2$. Eqn. 5.16 diverges at T_{SDW} as well. Inserting this result into Eqn. 5.14 gives:

$$\chi^{el}_{nem}(0) = \frac{1/r(T)}{1 - g \cdot 1/r(T)} = \frac{1}{r(T) - g} = \frac{1}{T - (T_{SDW} + g)} \tag{5.17}$$

This expression for χ^{el}_{nem} diverges not at T_{SDW} but at a temperature $T^* = T_{SDW} + g = T_{SDW} + \alpha/T^4_{SDW} > T_{SDW}$. However, the initial slope peaks at T_s. This discrepancy can be resolved by introducing a constant g' which accounts for magneto-elastic coupling and reads

$$g' = g + (\lambda^2_{sl})/c^s_0 \tag{5.18}$$

with the magneto-elastic constant λ_{sl} and the bare elastic constant c^s_0. Substituting this expression in Eqn. 5.17 yields the nematic susceptibility for magneto-elastic coupling [48]

$$\chi_{nem} = \frac{1}{T - (T_{SDW} + g')} \tag{5.19}$$

in which T_s is identified as $T_s = T_{SDW} + g' = T^* + \lambda^2_{sl}/c^s_0$.

Nematic susceptibility for $T_s > T > T_{SDW}$

One can find an expression for the free energy $F(\varphi)$ depending on the nematic order parameter φ as defined in Sec. 2.3. The free energy is then given in a Ginzburg-Landau like form by [17]

$$F(\varphi) = \frac{a(T)}{2}\varphi^2 + \frac{b}{4}\varphi^4 - h\varphi \tag{5.20}$$

with the distance from the structural transition $a(T) = T - T_s$. h is the conjugate field to the order parameter φ. The first two terms give the Mexican-hat potential for $a(T) < 0$. Minimising the free energy in Eqn. 5.20 yields

$$a(T)\varphi + b\varphi^3 - h = 0. \tag{5.21}$$

Derivation of Eqn. 5.21 with respect to h and noting that $\chi_{nem} = \partial\varphi/\partial h|_{h=0}$ results in an expression for the nematic susceptibility

$$\chi_{nem} = \frac{\partial\varphi}{\partial h}\,|_{h=0} = \frac{1}{a(T) + 3b\varphi^2}. \tag{5.22}$$

The nematic susceptibility dependent on temperature is then found by eliminating the order parameter φ. This can be achieved, as one considers the conjugate field h to be

zero within the nematic phase and substitutes $\varphi^2 = -a(T)/b$ resulting from Eqn. 5.21.

$$\chi_{\text{nem,orthorhombic}} = -\frac{1}{2a(T)} = -\frac{1}{2(T - T_s)} \tag{5.23}$$

In the tetragonal phase, $\varphi = 0$ holds and the nematic susceptibility is given by

$$\chi_{\text{nem,tetragonal}} = \frac{1}{a(T)} = \frac{1}{T - T_s} = -2\chi_{\text{nem,orthorhombic}} \tag{5.24}$$

which reproduces Eqn. 5.19.
The model is valid for small frequencies compared to the typical peak frequencies of the fluctuations. As the imaginary part of the Raman response function is proportional to the spin-nematic susceptibility, the initial slope of $R\chi''_{\text{fluct}}$ is the proper parameter to describe the fluctuations.

In conclusion, the additional spectral weight occurring in the B_{1g} symmetry was identified as a contribution due to fluctuations. These fluctuations were described in terms of two critical fluctuations with opposite momenta $\pm\mathbf{q}_c$. The occurrence solely in B_{1g} symmetry is consistent with the AL selection rules and the effective mass approximation. The combination of both approaches - AL selection rules and effective mass approximation - explained the lack of a fluctuation contribution in A_{1g} and B_{2g} symmetries. This pins down the ordering vector to be of the form of the SDW ordering vector $\mathbf{q}_c = (\pi, 0)$ as it connects Fermi sheets with the same sign of the form factor in the B_{1g} symmetry. Spin fluctuations were shown to be the driving force behind the magneto-structural phase transition in $Ba(Fe_{0.949}Co_{0.051})_2As_2$. The orthorhombic distortion at T_s is a manifestation of the symmetry breaking nematic ordering. The theoretical description given above in which a magneto-elastic coupling was introduced reproduced qualitatively the data in Fig. 5.7 (c). The picture of spin-driven nematicity is consistent with the approach of Fernandes *et al.* [17]. Fig. 5.13 shows the results of the $Ba(Fe_{0.949}Co_{0.051})_2As_2$ along with the results of an undoped $BaFe_2As_2$ sample and $Ba(Fe_{0.975}Co_{0.025})_2As_2$ in grey which were adapted from [18]. The nematic phase is shown in magenta and the boundary of the superconducting dome is defined by the results shown as blue squares [49].

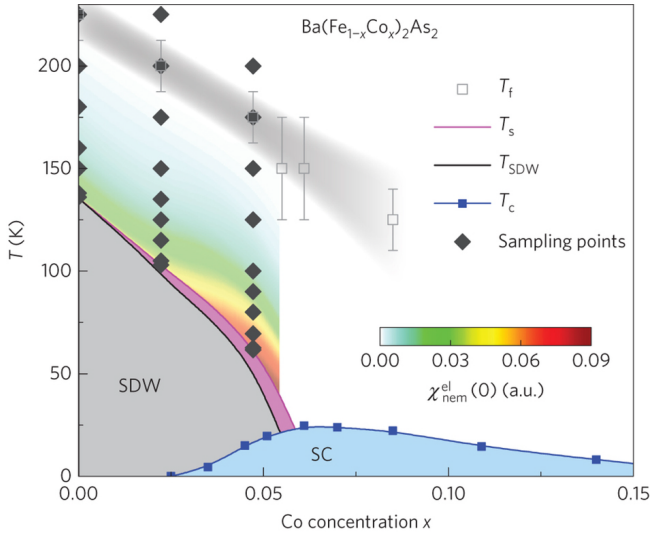

Figure 5.13.: Phase diagram of $Ba(Fe_{1-x}Co_x)_2As_2$. The nematic phase is depicted as magenta stripe. The blue squares indicate the boundaries of the superconducting dome as derived from [49]. Grey diamonds indicate the results from $BaFe_2As_2$ and $Ba(Fe_{0.975}Co_{0.025})_2As_2$ which were adapted from [12] and $Ba(Fe_{0.949}Co_{0.051})_2As_2$ the data obtained during this thesis. The grey field shows the temperature region at which the fluctuations set in. The field from green to red quantifies the magnitude of the initial slope as given by the scale in the region $T_f > T > T_{SDW}$. From [18].

As for the underdoped part of the phase diagram, the spin-nematic susceptibility increases rapidly close to the structural transition (see [12] for details). Yet the fluctuations increase strongly as one moves further towards the optimally doped region. It has to be pointed out that the theoretical description in the $Ba(Fe_{0.949}Co_{0.051})_2As_2$ does not entirely describe the behaviour of the spin-nematic susceptibility. It does not obey a Curie-Weiss-like law $|T - T_s|^{-1}$ as strictly as it does in the $BaFe_2As_2$ and $Ba(Fe_{0.975}Co_{0.025})_2As_2$ [18]. This indicates that spin fluctuations might not paint the entire picture as one approaches the quantum critical point.
Indications of fluctuations have been found for three doping concentrations $x > 0.051$ in earlier studies as well (see light grey boxes). Completing the phase diagram in the temperature regions closer to T_c for doping levels $x > 0.051$ may extend our current understanding of superconductivity for the iron based compounds.

6. Collective mode and intra band coupling in $Ba_{0.3}K_{0.7}Fe_2As_2$

The hole doped side of the phase diagram is similar to the electron doped side. Both have in common the existence of an SDW phase and the emergence of superconductivity. This chapter summarises the results of a study of $Ba_{0.3}K_{0.7}Fe_2As_2$. This sample is of interest as a generic change in the Raman spectra from $x = 0.48$ to $x = 0.62$ has been observed [50]. Also, a Lifshitz transition of the electron bands at the X and Y points has been discussed for doping levels $x > 0.8$ [20].
In Sec. 6.1 the determination of T_c is presented. This is followed by an illustration of the Raman data in Sec. 6.2 which underwent an analysis that can be found in Sec. 6.3. In Sec. 6.4 the results of the Raman data in $Ba_{0.3}K_{0.7}Fe_2As_2$ are compared to results from data obtained earlier [23, 50, 12]

6.1. Determination of T_c

The result of the T_c measurement for the $Ba_{0.3}K_{0.7}Fe_2As_2$ is presented in Fig. 6.1. As explained in Sec. 4.2 the third harmonic of the magnetic susceptibility $\chi(3f)$ was measured as a function of temperature with the sample exposed to an ac magnetic field of frequency f.

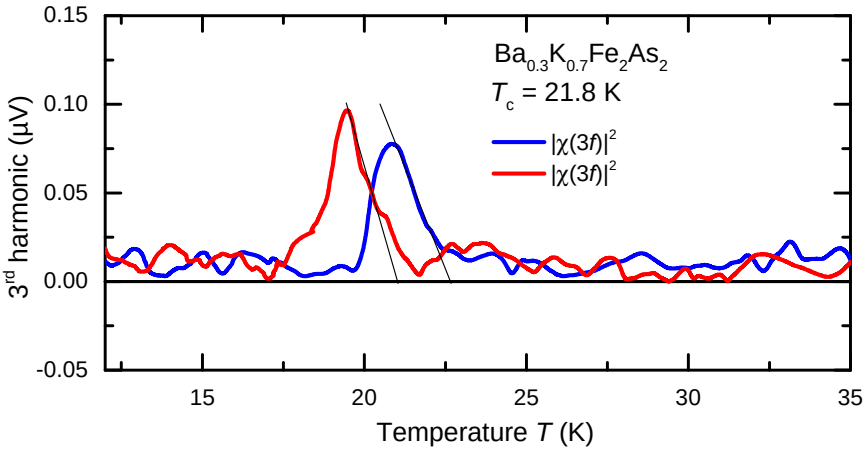

Figure 6.1.: T_c measurement of $Ba_{0.3}K_{0.7}Fe_2As_2$. The absolute squares of the third harmonic $|\chi(3f)|^2$ as a function f temperature for the warm-up in red and for the cool-down in blue are presented. The right flanks of the signals were linearly extrapolated towards $|\chi(3f)|^2 = 0$ (black lines) for both warm-up and cool-down.

The sample is firstly cooled well below T_c and then heated up again. Two sets of curves are obtained, which show an offset in temperature of about 2 K due to a finite heating/cooling rate. The finite rate results from a temperature gradient between the Pt resistor which measures the temperature and the sample. The linear trend of the maximum is extrapolated to zero. This yields two different temperatures T^{wu} and T^{cd} for the warm-up (wu) and the cool-down (cd) procedure. The average $T_c = 1/2(T^{wu} + T^{cd})$ is taken as we obtained similar heating/cooling rates. In the case of the $Ba_{0.3}K_{0.7}Fe_2As_2$ the extrapolations indicated by the black lines and their average yield $T_c = 21.8$ K. Raman spectra were obtained in the superconducting state, i. e. for temperatures $T < T_c$ and the normal state, i. e. $T > T_c$.

6.2. Experimental results of $Ba_{0.3}K_{0.7}Fe_2As_2$

Figure 6.2 (a) shows the experimental results of the Raman study on $Ba_{0.3}K_{0.7}Fe_2As_2$ in B_{1g} symmetry for temperatures below T_c. Along with these, one spectrum in the normal state is depicted in grey. The normal state shows no significant features and depends linearly on energy above 20 cm $^{-1}$. In comparison to that, the lowest temperature of the superconducting spectra at 8.0 K shows the opening of the superconducting gap for $\Omega < 30$ cm $^{-1}$. Two distinct features at 47 cm $^{-1}$ and 55 cm $^{-1}$ are present. Both features soften and damp as the temperature increases towards T_c. The second feature stays more prominent up to 14.0 K. At 16.0 K only the second features survives along with the suppression of spectral weight below 30 cm^{-1}. The superconducting and the normal state spectra converge around 70 cm $^{-1}$. This is consistent for all symmetries. The low energy response behaves linearly. In (b) the B_{2g} spectra show a small difference between superconducting and normal state. The prominent peak at 125 cm $^{-1}$ in the B_{2g} and A_{1g} symmetry is the E_g phonon [51] which is not influenced by the superconducting transition. In (c) the A_{1g} symmetry shows a peak at 54 cm $^{-1}$. The spectrum lacks the appearance of the smaller feature at 47 cm $^{-1}$. The A_{2g} spectrum in (d) is almost zero and is not discussed any further.

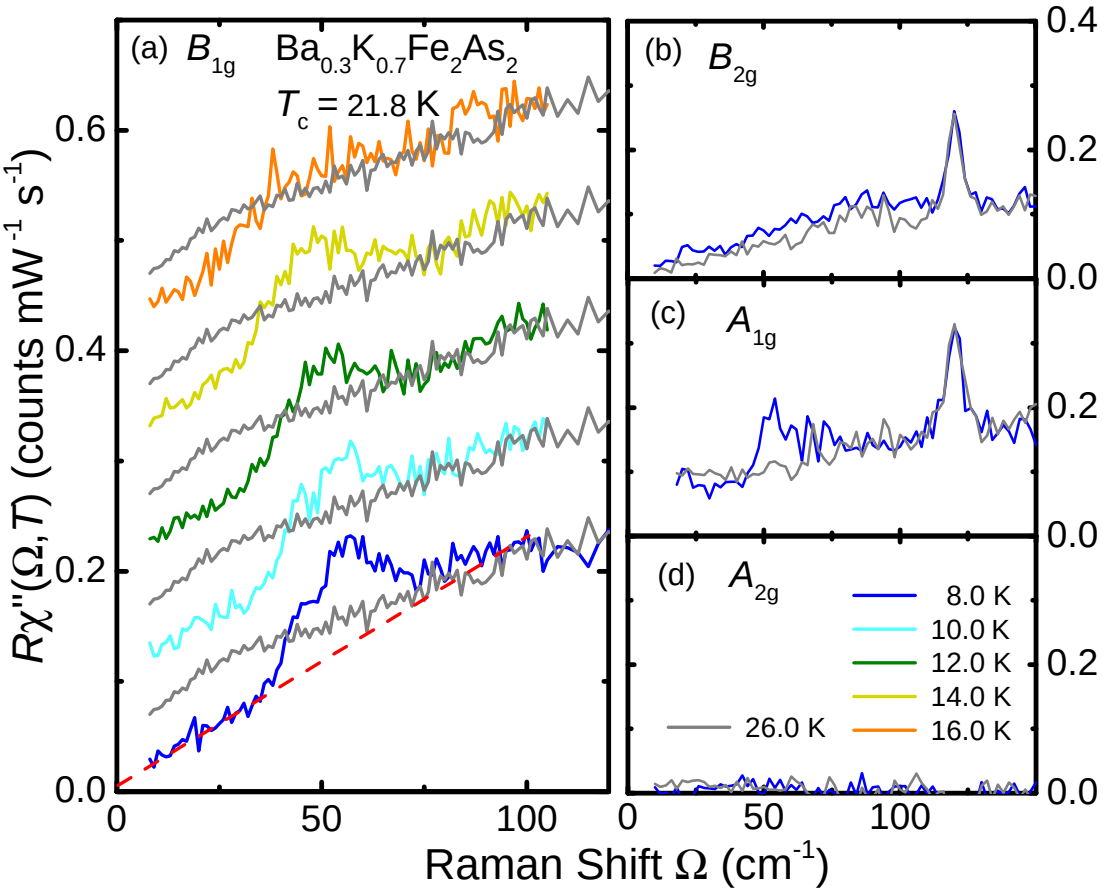

Figure 6.2.: Raman spectra for the $Ba_{0.3}K_{0.7}Fe_2As_2$ for various temperatures in the superconducting state with the temperatures as indicated along with one spectrum in the normal state in grey. (a) The B_{1g} spectra are shifted in y-direction for reasons of clarity in steps of 0.1. The dashed line in the 8.0 K spectrum represents exemplarily the linear response . (b) B_{2g} specta in the normal and the superconducting state with the E_g phonon at 125 cm $^{-1}$. (c) A_{1g} spectra with the E_g phonon at 125 cm $^{-1}$ and a prominent peak at approximately 54 cm $^{-1}$ in the superconducting state. (d) A_{2g} spectra which are zero for both the superconducting and the normal state.

6.3. Analysis

The B_{1g} spectra were subtracted with a linear background as indicated for the 8.0 K spectrum in Fig. 6.2 (a). The triangular symbol means the onset of the first feature, whereas the rectangular symbol marks the maximum of the second feature. In (b) both are shown along with the evolution of the BCS gap as a function of normalized temperature.

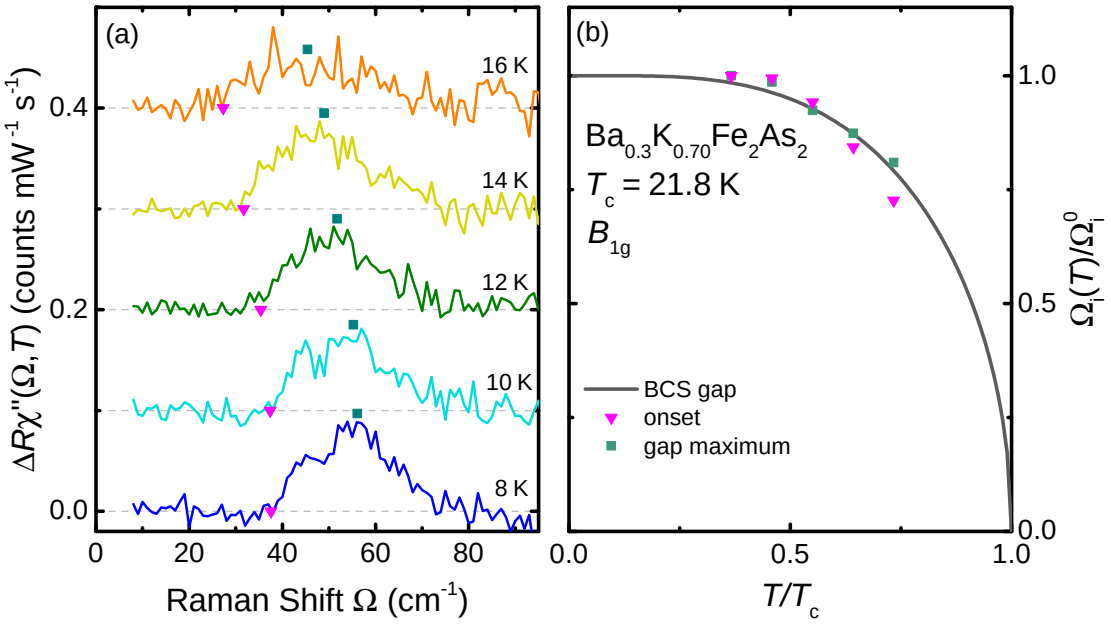

Figure 6.3.: (a) Subtracted Raman spectra for $T < T_c$. The triangular symbol means the onset of the first feature and the rectangular symbol marks the maximum of the second feature. (b) Features in the subtracted spectra along with the temperature evolution of the BCS gap.

This treatment of the data reveals a few details about the two features in B_{1g} symmetry. The onset survives up to 16.0 K whereas the smaller feature softens. One might argue, that the smaller feature might still be at the indicated position as the onset is still pronounced at approximately 22 cm $^{-1}$ at least for the 14.0 K spectrum. Nevertheless the behaviour of the smaller feature is consistent with the BCS temperature dependence of the gap for the other temperatures. The smaller feature does also not occur in A_{1g} symmetry which might indicate, that it is a BS mode. This will be discussed in the next section.

The second feature obeys the BCS gap evolution as well. As it appears in both A_{1g} and B_{1g} spectra, it is considered to be a pair breaking peak. From Fig. 6.5 (b) one finds the coupling to be weak ($\sim 3\ k_B T_c$).

6.4. Discussion

Fig. 6.4 (a) depicts the BZ of the 1Fe unit cell as already presented in Sec. 2.4 with the interaction in the dominant s-channel and the subdominant d-channel shown in green and blue. In (b) a Cooper pair forms within the lengthscale of the coherence length ξ along with the opening of the superconducting gap 2Δ.

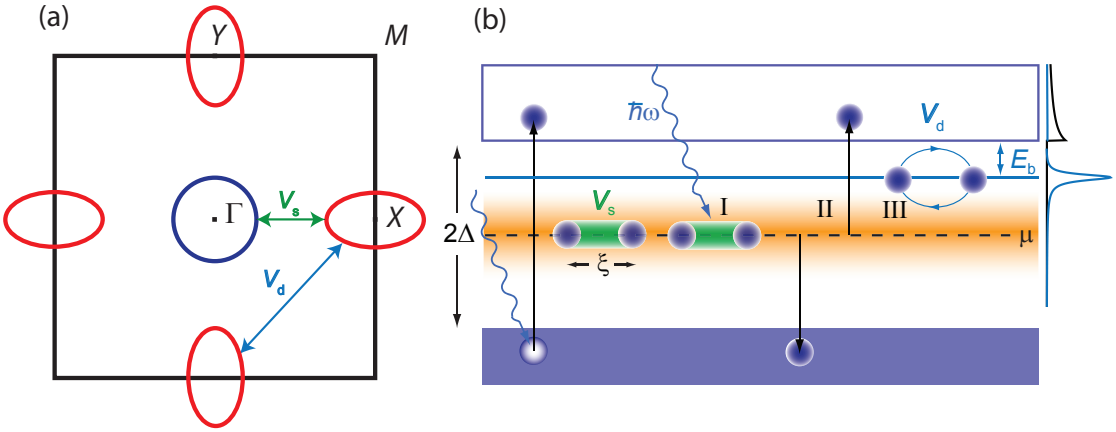

Figure 6.4.: Excitation of a Bardasis-Schrieffer mode. (a) BZ of the 1Fe unit cell in superconducting $Ba_{1-x}K_xFe_2As_2$ with round hole pockets at the Γ point and elliptical electron pockets at the X and Y point. V_s and V_d mean the interaction potential for s wave and d wave coupling. (b) The gap between these bands is 2Δ. The dashed line indicates the chemical potential μ. The energy scale on the left shows the mode resulting from the BS excitation (blue). Its energy is reduced by E_b with respect to the gap energy 2Δ depicted as black edge. From [52].

The pair can be broken up by a photon having the energy 2Δ as indicated by scenario I in the figure. This generates a response similar to the black curve at the very right of (b) with the pair breaking peak at 2Δ. The Cooper pair splits up (II). Electrons which stay in a region comparable to the coherence length ξ can recombine to a bound state with energy E_b. This happens due to the existence of the subdominant pairing potential

V_d (blue) as illustrated in III. A relation between V_d and E_b is given by [46]

$$\frac{E_b}{2\Delta} \approx \left(\frac{V_d}{V_s}\right)^2. \tag{6.1}$$

The emergent mode in the Raman spectrum is called a Bardasis-Schrieffer (BS) mode, the occurrence of which was predicted for the B_{1g} symmetry in iron pnictides [25]. The BS mode was much stronger observed at other doping levels as indicated in Fig. 6.5. In the following the results of the $Ba_{0.3}K_{0.7}Fe_2As_2$ are compared with the results found earlier for other doping concentrations [12, 46, 50].
In (a) the B_{1g} difference spectrum $\Delta R\chi''(\Omega, T)$ of the $Ba_{0.3}K_{0.7}Fe_2As_2$ is shown along with difference spectra of samples with doping levels reaching from $x = 0.35$ to $x = 0.62$. Difference spectra means here $\Delta R\chi''(\Omega, T) = R\chi''(\Omega, T << T_c) - R\chi''(\Omega, T > T_c)$. The arrows indicate the pair breaking peak from s-wave coupling (green), the BS mode resulting from the pairing potential V_d (blue) and the gap on the outer hole band (dark blue). The peak of the outer hole band shifts to lower energies as doping increases and vanishes for the two doping levels $x \geq 0.62$. The spectral weight of the BS mode results from the Bardasis-Schrieffer mechanism described above [46]. The BS mode occurs firstly for $x = 0.35$ and shifts towards lower energies upon increased doping. Between $x = 0.48$ and $x = 0.62$ another peak evolves at the position indicated by the asterisk and survives further doping towards $x = 0.7$. Fig. 6.5 (b) illustrates the similarities between the $Ba_{0.38}K_{0.62}Fe_2As_2$ and $Ba_{0.3}K_{0.7}Fe_2As_2$ spectra in B_{1g}, B_{2g} and A_{1g} symmetries. The peaks at $\sim 3\ k_B T_c$ most likely correspond to the BS mode already found for doping levels $0.35 < x \leq 0.48$ for both, $Ba_{0.38}K_{0.62}Fe_2As_2$ and $Ba_{0.3}K_{0.7}Fe_2As_2$ as they occur only in B_{1g} symmetry. But compared to the samples of lower doping the mode weakens considerably which hints towards a decay of the inter band scattering from the V_d coupling.

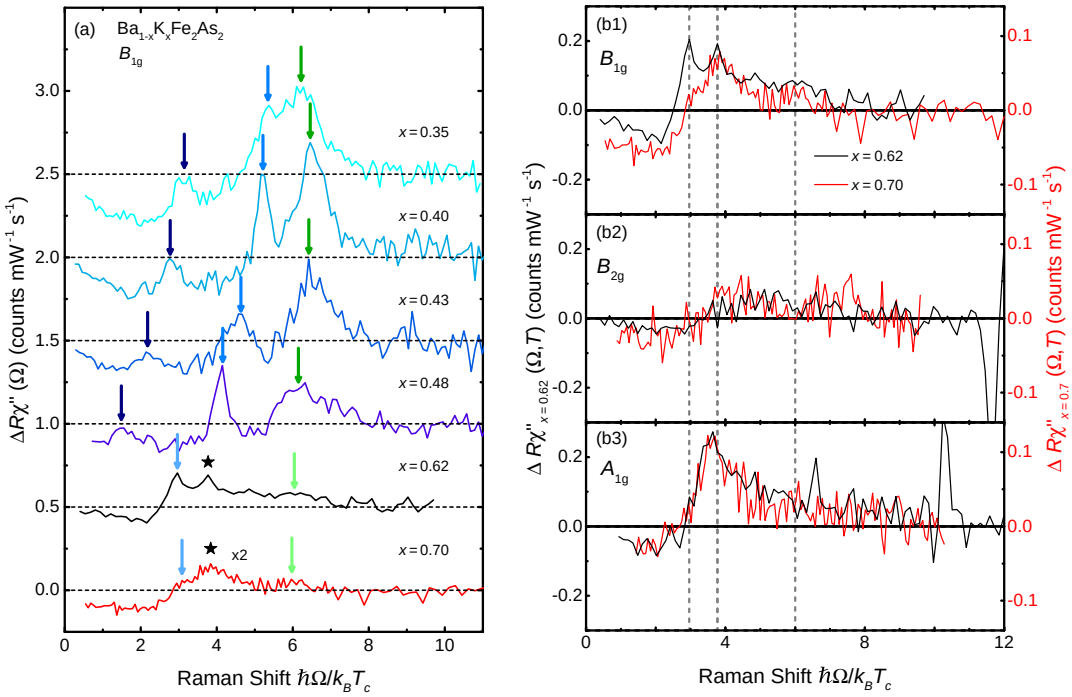

Figure 6.5.: $Ba_{0.3}K_{0.7}Fe_2As_2$ data in comparison with $Ba_{1-x}K_xFe_2As_2$ samples of indicated doping x. (a) Difference spectra $\Delta R\chi''(\Omega, x)$ in B_{1g} symmetry normalised to their respective T_c. The spectra are shifted for reasons of clarity and the dashed lines represent zero. Green arrows indicate the pair breaking peaks. Blue arrows show the position of the BS mode. Dark blue arrows represent the gap on the outer hole band. The asterisks indicate features the origin of which has not been clarified. The $Ba_{0.3}K_{0.7}Fe_2As_2$ spectra was multiplied by a factor of 2. (b1-b3) Difference spectra $\Delta R\chi''(\Omega, x)$ of the $Ba_{0.3}K_{0.7}Fe_2As_2$ and $Ba_{0.38}K_{0.62}Fe_2As_2$ for indicated symmetries. Spectra of $x = 0.35$ to $x = 0.62$ from [50, 12, 23].

The coupling strength of V_d is also proportional to the amount of spectral weight shifted from the superconducting peak into the BS mode. This would be consistent with ARPES results which suggest the electron bands at the X and Y points to vanish towards a doping concentration of $x = 0.8$ [20]. This scenario is supported by a weakening of the pair breaking peak at $6 - 7\ k_BT_c$ resulting from the s-coupling. Shrinking of the electron pockets could worsen the inter band nesting necessary for the arising of superconductivity through the s-channel and yield the weakening of the pair breaking

peak in the difference spectra. Additionally, the evolution of a linear response in the low energy spectrum points towards the existence of a nodal gap. The existence of nodes on the gap yield scattering processes below the energy of 2Δ and thus a non-vanishing response in the Raman spectrum. This is in contrast to the rather isotropic gaps of the optimally doped samples.
The peak designated by the asterisk appears in B_{1g} and A_{1g} symmetry. Its occurrence in the difference spectra of the $Ba_{0.38}K_{0.62}Fe_2As_2$ coincides with the vanishing of the gap from the outer hole band going from $x = 0.48$ to $x = 0.62$ (cf. 6.5 (a)). The peak could be the result of weak coupling intra band scattering from this outer hole band. In this scenario, the outer hole band would conserve superconductivity and carry it towards $x = 1$. This picture would be consistent with the occurrence of superconductivity in KFe_2As_2 with $T_c \sim 4$ K.

7. Summary

In the course of this thesis, Raman data were obtained and analysed of the electron doped $Ba(Fe_{0.949}Co_{0.051})_2As_2$ and the hole doped $Ba_{0.3}K_{0.7}Fe_2As_2$ at different temperatures.
While both samples exhibit superconductivity, the focus in the $Ba(Fe_{0.949}Co_{0.051})_2As_2$ was placed on the structural and the magnetic transitions at $T_s = 60.9$ K and $T_{SDW} = 50.0$ K, respectively. Particularly, the region close to T_s and T_{SDW} was of special interest because of the strong response from spin fluctuations. In order to extract the bare fluctuation contribution to the overall Raman response, it was necessary to pin down the onset temperature T_f, which was done by comparison of the Raman relaxation rates with transport measurements. The temperature dependent particle-hole continua were approximated with a model and subsequently subtracted from the Raman response yielding the bare fluctuation contribution. The response was described in terms of an exchange of two critical fluctuations with finite opposite momenta $\pm\mathbf{q}_c$, as first studied theoretically by Aslamazov and Larkin. The Aslamazov-Larkin treatment entails selection rules which require the Raman vertex to have the same sign on both ends of the critical vector $\mathbf{q}_c$ for the response to be finite. Otherwise these contributions cancel out. Under consideration of these selection rules the ordering vector for the contributions was determined to be $(\pi, 0)$ which is the SDW ordering vector. As the fluctuations survive the structural transition and only vanish upon magnetic ordering, a connection between magnetic ordering and nematic fluctuations can be drawn. While the theoretical framework of Karahasanovic *et al.* [47] accounts for the Curie-Weiss-like behaviour of the fluctuations in $BaFe_2As_2$ and $Ba(Fe_{0.975}Co_{0.025})_2As_2$, this was not verified for the $Ba(Fe_{0.949}Co_{0.051})_2As_2$. The Raman susceptibility $\tilde{R}(\Omega)$ was found to be proportional to the electronic contribution of the nematic susceptibility yielding a maximum at T_s, but it does not strictly obey $\tilde{R}(\Omega) \propto |T - T^*|^{-1}$. The initial slope peaks at a higher value and could indicate, that the fluctuations are stronger in $Ba(Fe_{0.949}Co_{0.051})_2As_2$. This could point toward an additional contributions to the fluctuations resulting from the superconducting ground state. Nevertheless, spin-fluctuations were able to be pinned down as the underlying cause for structural and magnetic phase transition and the

appearance of the nematic phase in $Ba(Fe_{0.949}Co_{0.051})_2As_2$. Further clarification can be expected if higher doping levels are studied, particularly with optimally doped and over doped samples in which the magnetic and structural transitions are not present. In the light of inter band spin fluctuations we studied the hole-doped compound $Ba_{0.3}K_{0.7}Fe_2As_2$. This sample is especially interesting as the electron bands are expected to vanish at a doping concentration of $x = 0.8$ [20] and possible spin fluctuation have not been detected. A symmetry and temperature study was conducted to analyse superconductivity induced features. A comparison with samples around optimal doping showed a decay of the typical coupling strength from intermediate coupling ($2\Delta/k_BT_c \sim 7$) to weak coupling ($2\Delta/k_BT_c \sim 3$) which suggests a generic change in the superconducting gap structure. The evolution of a linear response in B_{1g} symmetry for small energies but several temperatures supports this assumption as it indicates the existence of a nodal gap in contrast to the optimally doped samples showing very isotropic gaps. But there are also similarities with samples of lower doping. A narrow mode was identified with a BS mode as present in various lower doping. However a considerable weakening of this mode hints to a decay of inter band scattering in proximity of the transition at a doping of $x = 0.8$. It was thus suggested that the most prominent superconducting feature could emerge from weak coupling intra band scattering at the extended hole bands which could carry superconductivity towards the KFe_2As_2 compound with $x = 1$.

A. Control box Raman Lab I

The figures below show schematics of the new control box in the Raman Lab I. The circuit diagram shows the wiring within the box explicitly. MM1 and MM2 mean the two 10x2 clamps (2 card slots with 10 channels each of which with two contacts High-Low H-L) in the new Digital Multi Meter (DMM). The control box connects the DMM with the interior of the cryostat.

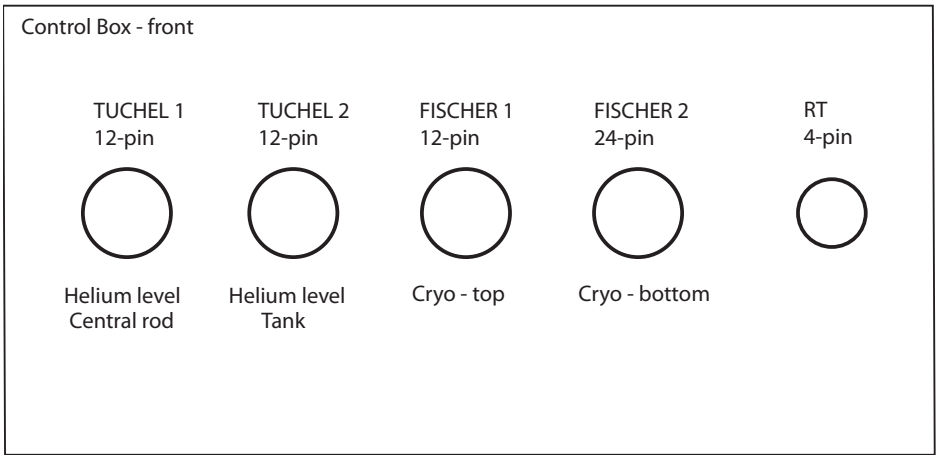

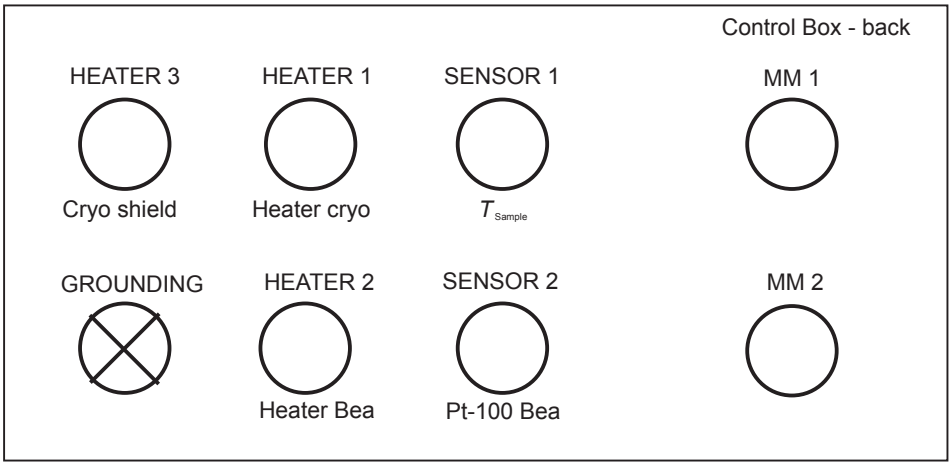

Box

DMM

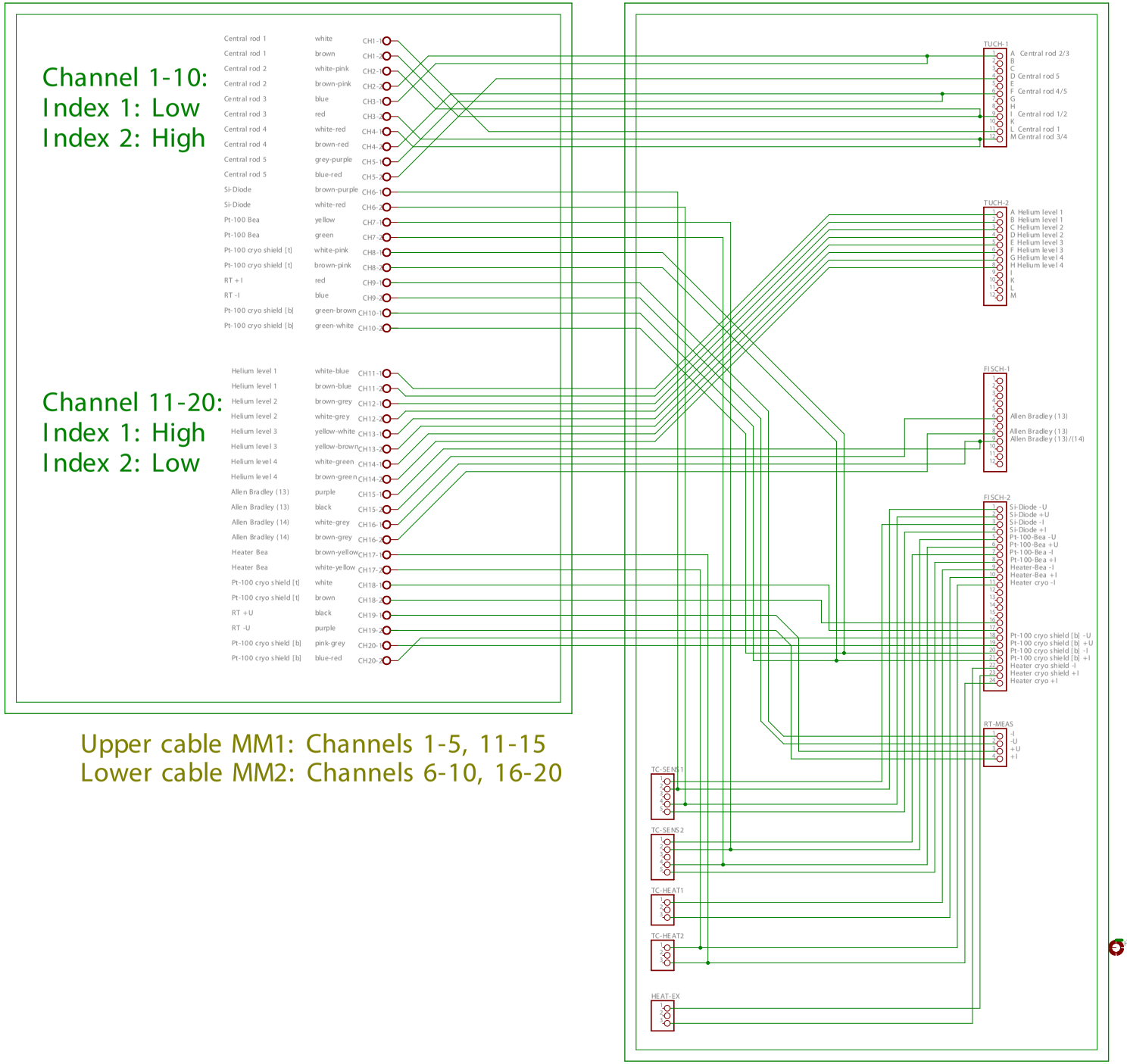

Upper cable MM1: Channels 1-5, 11-15
Lower cable MM2: Channels 6-10, 16-20

Channel 1-10:
Index 1: Low
Index 2: High

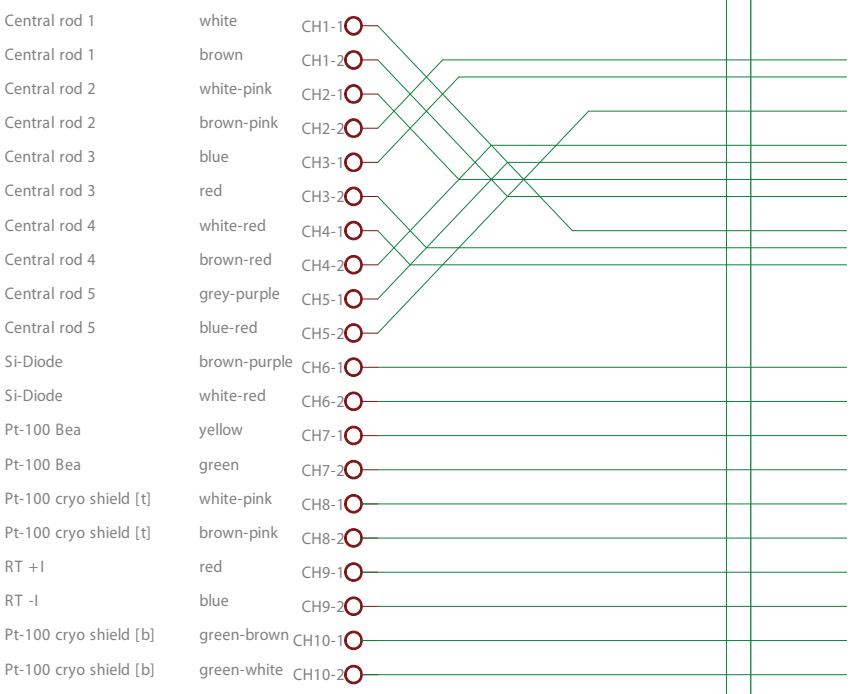

Channel 11-20:
Index 1: High
Index 2: Low

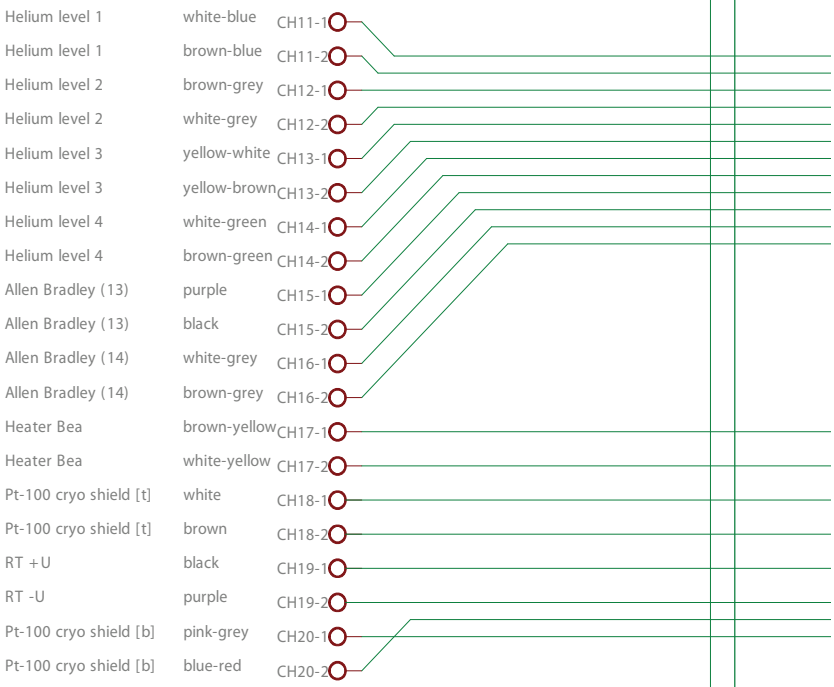

Upper cable MM1: Channels 1-5, 11-15
Lower cable MM2: Channels 6-10, 16-20

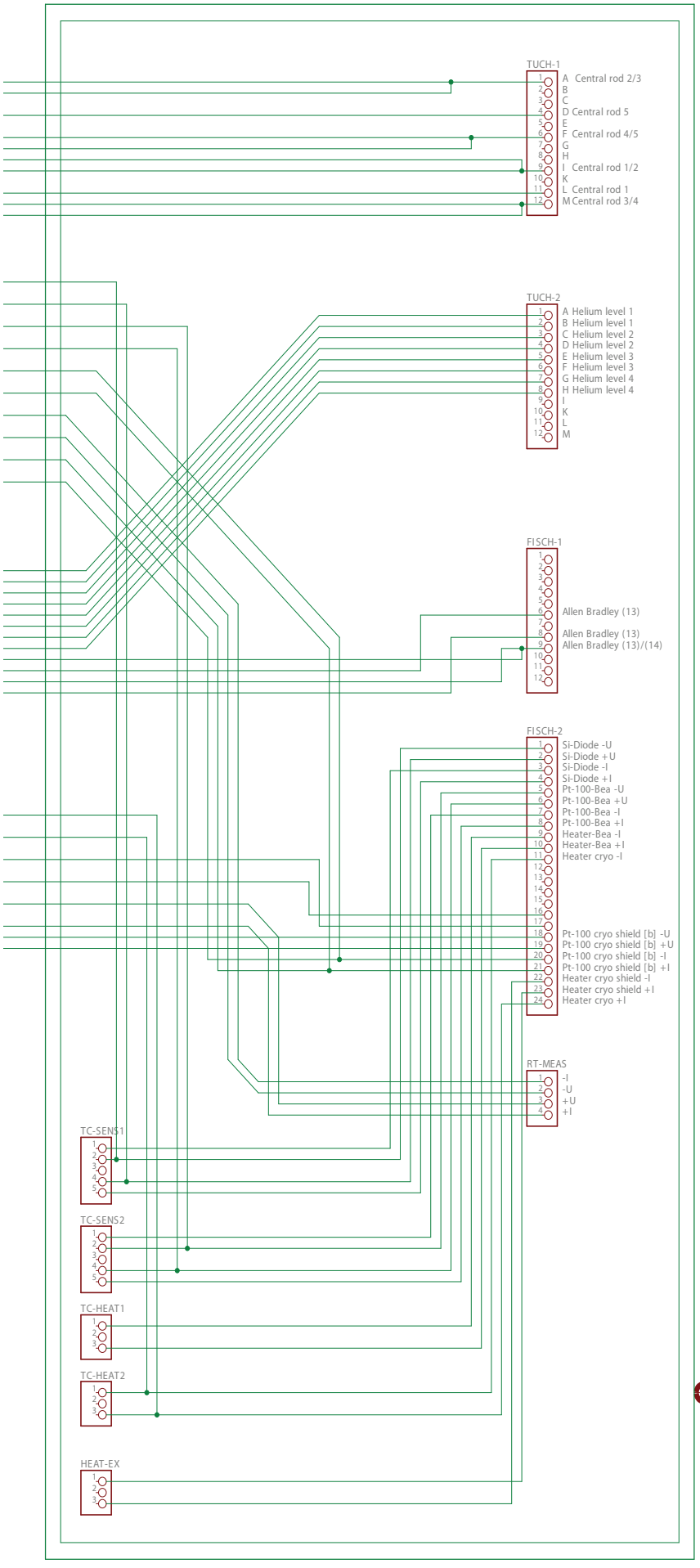
TUCH-1
A Central rod 2/3
B
C
D Central rod 5
E
F Central rod 4/5
G
H
I Central rod 1/2
K
L Central rod 1
M Central rod 3/4
TUCH-2
A Helium level 1
B Helium level 1
C Helium level 2
D Helium level 2
E Helium level 3
F Helium level 3
G Helium level 4
H Helium level 4
I
K
L
M
FISCH-1
Allen Bradley (13)
Allen Bradley (13)
Allen Bradley (13)/(14)
FISCH-2
Si-Diode -U
Si-Diode +U
Si-Diode -I
Si-Diode +I
Pt-100-Bea -U
Pt-100-Bea +U
Pt-100-Bea -I
Pt-100-Bea +I
Heater-Bea -I
Heater-Bea +I
Heater cryo -I
Pt-100 cryo shield [b] -U
Pt-100 cryo shield [b] +U
Pt-100 cryo shield [b] -I
Pt-100 cryo shield [b] +I
Heater cryo shield -I
Heater cryo shield +I
Heater cryo +I
RT-MEAS
-I
-U
+U
+I
TC-SENS1
TC-SENS2
TC-HEAT1
TC-HEAT2
HEAT-EX
PE

Bibliography

[1] H. K. Onnes, *Further experiments with liquid helium D - On the change of the electrical resistance of pure metals at very low temperatures, etc V The disappearance of the resistance of mercury*, Proc. K. Ned. Akad. Wet **14**, 113 (1911).

[2] A. P. Drozdov, M. I. Eremets, I. A. Troyan, V. Ksenofontov, and S. I. Shylin, *Conventional superconductivity at 203 kelvin at high pressures in the sulfur hydride system*, Nature **525**, 73 (2015), letter.

[3] J. Bardeen, L. N. Cooper, and J. R. Schrieffer, *Theory of Superconductivity*, Phys. Rev. **108**, 1175 (1957).

[4] J. G. Bednorz and K. A. Müller, *Possible high T_c superconductivity in the Ba-La-Cu-O System*, Z. Phys. B **64**, 189 (1986).

[5] Y. Kamihara, H. Hiramatsu, M. Hirano, R. Kawamura, H. Yanagi, T. Kamiya, and H. Hosono, *Iron-Based Layered Superconductor: LaOFeP*, J. Am. Chem. Soc.. **128**, 10012 (2006), pMID: 16881620.

[6] Y. Kamihara, T. Watanabe, M. Hirano, and H. Hosono, *Iron-Based Layered Superconductor La[O1-xFx]FeAs (x = 0.05â^'0.12) with Tc = 26 K*, Journal of the American Chemical Society **130**, 3296 (2008), pMID: 18293989.

[7] R. Hackl and W. Hanke, *Towards a better understanding of superconductivity at high transition temperatures* , Eur. Phys. J. ST **188**, 3 (2010).

[8] J.-H. Chu, H.-H. Kuo, J. G. Analytis, and I. R. Fisher, *Divergent Nematic Susceptibility in an Iron Arsenide Superconductor*, Science **337**, 710 (2012).

[9] J. Paglione and R. L. Greene, *High-temperature superconductivity in iron-based materials*, Nat. Phys. **6**, 645 (2010).

[10] M. Rotter, M. Tegel, and D. Johrendt, *Superconductivity at 38 K in the Iron Arsenide $(Ba_{1-x}K_x)Fe_2As_2$*, Phys. Rev. Lett. **101**, 107006 (2008).

[11] I. I. Mazin, T. P. Devereaux, J. G. Analytis, J.-H. Chu, I. R. Fisher, B. Muschler, and R. Hackl, *Pinpointing gap minima in $Ba(Fe_{0.94}Co_{0.06})_2As_2$ via band-structure calculations and electronic Raman scattering*, Phys. Rev. B **82**, 180502 (2010).

[12] F. Kretzschmar, Dissertation, Technische Universität München, 2015.

[13] B. Muschler, priv. comm., 2012.

[14] H. Wadati, I. Elfimov, and G. A. Sawatzky, *Where Are the Extra d Electrons in Transition-Metal-Substituted Iron Pnictides?*, Phys. Rev. Lett. **105**, 157004 (2010).

[15] A. E. Böhmer, P. Burger, F. Hardy, T. Wolf, P. Schweiss, R. Fromknecht, M. Reinecker, W. Schranz, and C. Meingast, *Nematic Susceptibility of Hole-Doped and Electron-Doped* $BaFe_2As_2$ *Iron-Based Superconductors from Shear Modulus Measurements*, Phys. Rev. Lett. **112**, 047001 (2014).

[16] P. J. Hirschfeld, M. M. Korshunov, and I. I. Mazin, *Gap symmetry and structure of Fe-based superconductors*, Rep. Prog. Phys. **74**, 124508 (2011).

[17] C. A. V. Fernandes, R. M. and J. Schmalian, *What drives neamtic order in iron-based superconductors?*, Nature Physics **10**, 97 (2014).

[18] F. Kretzschmar, T. Bohm, U. Karahasanovic, B. Muschler, A. Baum, D. Jost, J. Schmalian, S. Caprara, M. Grilli, C. Di Castro, J. G. Analytis, J.-H. Chu, I. R. Fisher, and R. Hackl, *Critical spin fluctuations and the origin of nematic order in Ba(Fe1-xCox)2As2*, Nat Phys **advance online publication**, (2016), letter.

[19] Y. Sekiba, T. Sato, K. Nakayama, K. Terashima, P. Richard, J. H. Bowen, H. Ding, Y.-M. Xu, L. J. Li, G. H. Cao, Z.-A. Xu, and T. Takahashi, *Electronic structure of heavily electron-doped $BaFe_{1.7}Co_{0.3}As_2$ studied by angle-resolved photoemission*, New J. Phys. **11**, 025020 (2009).

[20] N. Xu, P. Richard, X. Shi, A. van Roekeghem, T. Qian, E. Razzoli, E. Rienks, G.-F. Chen, E. Ieki, K. Nakayama, T. Sato, T. Takahashi, M. Shi, and H. Ding, *Possible nodal superconducting gap and Lifshitz transition in heavily hole-doped $Ba_{0.1}K_{0.9}Fe_2As_2$*, Phys. Rev. B **88**, 220508 (2013).

[21] C. Fang, H. Yao, W.-F. Tsai, J. Hu, and S. A. Kivelson, *Theory of electron nematic order in LaFeAsO*, Phys. Rev. B **77**, 224509 (2008).

[22] C. Xu, M. Müller, and S. Sachdev, *Ising and spin orders in the iron-based superconductors*, Phys. Rev. B **78**, 020501 (2008).

[23] T. Böhm, private communication (PUBLISHER, 2016).

[24] R. Gross and A. Marx, *Festkörperphysik* (Oldenbourg Wissenschaftsverlag, 2012).

[25] W.-C. Lee, S.-C. Zhang, and C. Wu, *Pairing State with a Time-Reversal Symmetry Breaking in FeAs-Based Superconductors*, Phys. Rev. Lett. **102**, 217002 (2009).

[26] D. J. Scalapino and T. P. Devereaux, *Collective d-wave exciton modes in the calculated Raman spectrum of Fe-based superconductors*, Phys. Rev. B **80**, 140512 (2009).

[27] T. Devereaux and R. Hackl, *Inelastic light scattering from correlated electrons*, Rev. Mod. Phys. **79**, 175 (2007).

[28] A. Baum, Diplomarbeit, WMI, TU Muenchen, 2012.

[29] H. Nyquist, *Thermal Agitation of Electric Charge in Conductors*, Phys. Rev. **32**, 110 (1928).

[30] D. Pines and Nozières, *The Theory of Quantum Liquids: Normal Fermi Liquids* (Addison-Wesley, New-York, 1966).

[31] D. Einzel and R. Hackl, *Electronic Raman Scattering in Copper Oxide Superconductors*, J. Raman Spectrosc. **27**, 307 (1996).

[32] B. Muschler, Phd thesis, WMI, TU Muenchen, 2012.

[33] M. Opel, Diplomarbeit, Walther-Meissner-Institut, 1995.

[34] M. Opel, Dissertation, Technische Universität München, 2000.

[35] T. Böhm and A. Baum, *Die neue Spektrometersteuerung*, Walther-Meißner-Institut, 2012.

[36] B. Muschler, Diplomarbeit, WMI, TU Muenchen, 2007.

[37] F. Venturini, Dissertation, Technische Universität München, 2003.

[38] S. Shatz, A. Shaulov, and Y. Yeshurun, *Universal behavior of harmonic susceptibilities in type-II superconductors*, Phys. Rev. B **48**, 13871 (1993).

[39] C. P. Bean, *Magnetization of Hard Superconductors*, Phys. Rev. Lett. **8**, 250 (1962).

[40] M. Opel, R. Nemetschek, C. Hoffmann, R. Philipp, P. F. Müller, R. Hackl, I. Tüttõ, A. Erb, B. Revaz, E. Walker, H. Berger, and L. Forró, *Carrier relaxation, pseudogap, and superconducting gap in high-T_c cuprates: A Raman scattering study*, Phys. Rev. B **61**, 9752 (2000).

[41] W. Götze and P. Wölfle, *Homogeneous Dynamical Conductivity of Simple Metals*, Phys. Rev. B **6**, 1226 (1972).

[42] S. Caprara, C. Di Castro, M. Grilli, and D. Suppa, *Charge-Fluctuation Contribution to the Raman Response in Superconducting Cuprates*, Phys. Rev. Lett. **95**, 117004 (2005).

[43] N. E. Hussey, J. C. Alexander, and R. A. Cooper, *Optical response of high-T_c cuprates: Possible role of scattering rate saturation and in-plane anisotropy*, Phys. Rev. B **74**, 214508 (2006).

[44] L. Aslamasov and A. Larkin, *The influence of fluctuation pairing of electrons on the conductivity of normal metal*, Phys. Rev. A **26**, 238 (1968).

[45] Y. Gallais, R. M. Fernandes, I. Paul, L. Chauvière, Y.-X. Yang, M.-A. Méasson, M. Cazayous, A. Sacuto, D. Colson, and A. Forget, *Observation of Incipient Charge Nematicity in* $Ba(Fe_{1-X}Co_X)_2As_2$, Phys. Rev. Lett. **111**, 267001 (2013).

[46] T. Böhm, A. F. Kemper, B. Moritz, F. Kretzschmar, B. Muschler, H.-M. Eiter, R. Hackl, T. P. Devereaux, D. J. Scalapino, and H.-H. Wen, *Balancing Act: Evidence for a Strong Subdominant d-Wave Pairing Channel in* $Ba_{0.6}K_{0.4}Fe_2As_2$, Phys. Rev. X **4**, 041046 (2014).

[47] U. Karahasanovic, F. Kretzschmar, T. Böhm, R. Hackl, I. Paul, Y. Gallais, and J. Schmalian, *Manifestation of nematic degrees of freedom in the Raman response function of iron pnictides*, Phys. Rev. B **92**, 075134 (2015).

[48] H. Kontani and Y. Yamakawa, *Linear Response Theory for Shear Modulus C_{66} and Raman Quadrupole Susceptibility: Evidence for Nematic Orbital Fluctuations in Fe-based Superconductors*, Phys. Rev. Lett. **113**, 047001 (2014).

[49] J.-H. Chu, J. G. Analytis, C. Kucharczyk, and I. R. Fisher, *Determination of the phase diagram of the electron-doped superconductor $Ba(Fe_{1-x}Co_x)_2As_2$*, Phys. Rev. B **79**, 014506 (2009).

[50] M. Rehm, Masterarbeit, WMI, TU Muenchen, 2015.

[51] A. P. Litvinchuk, V. G. Hadjiev, M. N. Iliev, B. Lv, A. M. Guloy, and C. W. Chu, *Raman-scattering study of* $K_xSr_{1-x}Fe_2As_2$ *(x = 0.0,0.4)*, Phys. Rev. B **78**, 060503 (2008).

[52] F. Kretzschmar, B. Muschler, T. Böhm, A. Baum, R. Hackl, H.-H. Wen, V. Tsurkan, J. Deisenhofer, and A. Loidl, *Raman-Scattering Detection of Nearly Degenerate s-Wave and d-Wave Pairing Channels in Iron-Based* $Ba_{0.6}K_{0.4}Fe_2As_2$ *and* $Rb_{0.8}Fe_{1.6}Se_2$ *Superconductors*, Phys. Rev. Lett. **110**, 187002 (2013).

Acknowledgements

There are many people to thank of whom only a handful fit on this page. So I might as well keep it short and thank

- **Prof. Dr. Rudolf Gross** for the opportunity to perform the measurements and the entire thesis in the great environment offered by the WMI.
- **PD Dr. Rudi Hackl** for basically everything, especially the discussions and explanations as well as the valuable input whenever we got stuck. Without him we would be a bunch of confused dogs chasing their own tails.
- **Prof. Dietrich Einzel** for valuable discussions about Raman spectroscopy in general and collective mode excitations in particular.
- **Dr. Florian Kretzschmar** for giving me the opportunity to participate in his discovery and for pulling me off my horse.
- **Thomas Böhm** for reminding me why I had been studying physics in the first place, for the excellent discussions and explanations and for being so patient when I displayed my stubbornness every once in a while.
- the guys of the Raman group **Nitin Chelwani**, **Andreas Baum** and **Ramez al-Housseini** for the fantastic team atmosphere and support. Particularly **David Hoch** for his friendship during the last year.
- my roomies **Michaela Lammel**, **Richard Schlitz**, **Philip Louis**, **Miriam Müting** and **the dog** and of course all the other Master and PhD students for making this year gone by a good deal faster than expected.
- the helium guys **Peter Binkert**, **Jan Naundorf** and **Harald Schwaiger** for securing the supply with helium and nitrogen and **Jan** for all the cigarettes.
- **Sybilla Plöderl** and **Maria Botta** for the occasional reminder that we sit a bit too often quite high up the ivory tower.

- **all the folks I probably forgot here**.
- my family, particularly my mother **Claudia** and my siblings **Sabine** and **Thorsten**. Thanks also to the other members of the quite huge **Jost** family for the enduring support not only over the last but the last few years.

I feel special gratitude towards the two people who pushed me towards physics

- **Kerstin** and **Christian Wallner** who have been sponsoring me and giving me guidance in more than one regard for almost a decade now.

And then there is this person whose friendship I so dearly missed. I am very grateful, that you had the courage to take this step and gifted me with the contentment and support which carried me over the finish line.

"No pain, no gain."